TECHNIQUES AND INSTRUMENTATION IN ANALYTICAL CHEMISTRY—VOLUME 8

NUCLEAR ANALYTICAL TECHNIQUES IN MEDICINE

Edited by

Roberto Cesareo

Università degli Studi di Roma "La Sapienza", Centro per l'Ingegneria Biomedica, 00186 Rome, Italy

ELSEVIER
Amsterdam – Oxford – New York – Tokyo 1988

Chapter 5

SCATTERING OF LOW ENERGY X- OR GAMMA MONOENERGETIC RADIATION

GIOVANNI E. GIGANTE
Centro per l'Ingegneria Biomedica
Università di Roma "La Sapienza" e
Dipartimento di Scienze Biomediche
Facoltà di Medicina e Chirurgia, 67100 L'Aquila (Italy)

5.1 INTRODUCTION

Many researchers concerned in transmission techniques have wondered whether scattered photons, produced simultaneously in the sample, could be used to obtain analytical information complementary or of better quality than that obtained by the transmitted photons.

They know that the Compton scattering is directly related to the electron density and that the coherent scattering strongly depends upon the atomic number of the target. However, they also know that the intensity of the scattered radiation is low compared to transmitted radiation.

It is worthwhile pointing out (see Fig. 5.1) that the volume from which the scattered photons emerge, is only a small portion of the total volume crossed by the primary photon beam. Moreover, the fluence of photons through an angle is proportional to the differential scattering cross-section, which is only a small fraction of the total collision cross-section.

However, this kind of technique is not frequently used for several reasons, and mainly because of the extraordinary analytical power of absorptiometric techniques that in many cases lead to satisfactory results with the adjustment of few physical parameters and the use of suitable methods of measurement.

Nevertheless, after an early enthusiasm, the normal attitude of most research workers is of skepticism regarding the use of scattered radiation in solving analytical problems. This attitude is mainly due to the number of physical and geometrical parameters to be studied and optimized in a technique using scattered photons. Actually, the use of these techniques is hardly ever immediate, on account of a series of experimental obstacles.

However, during the last decade many analytical techniques using the detection of scattered photons have been suggested. They have been proposed

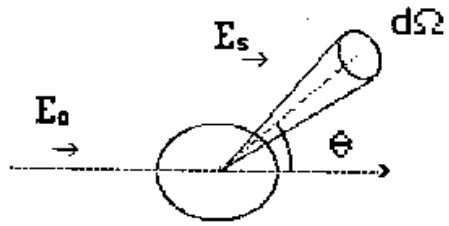

Fig. 5.1. Scattering of a narrow primary photon beam from a monoelemental target. The scattered photons into a solid angle ($d\Omega$) can be calculated through the differential cross-section ($d\sigma/d\Omega$) for the scattering processes.

for the "in vitro" and "in vivo" measurement of physical parameters such as the effective atomic number (Ze), mass (ρ) (or the electronic (ρ_e)) density of the sample and the sample mass or thickness.

The most interesting medical application of scattering techniques is that of tissue characterization. This is a typical analytical problem in which one or more physical parameters have been considered as representative of the tissue state. To give an example, if a parameter assumes a value in a certain range the tissue is healthy, while if it falls in another range, the tissue is affected by a particular disease. Unfortunately, as already observed in the case of bone disease the definition of the interval of values corresponding to a particular state, is not easy. In fact, a large amount of accurate data is needed to establish a good statistical significance of the different interval limits.

This topic was introduced in connection with the computed tomography techniques (CT); then it was extensively studied by means of other imaging techniques, with a special effort for ultrasounds. It should be stressed that in tissue characterization an absolute measurement is required. Therefore, only analytical techniques having good performance, especially "in vivo", in terms of sensitivity, precision, and accuracy may be used.

The photon scattering techniques, referred to below as P.S.T., can be subdivided into two main classes according to the energy resolution of the detector used. One class includes the techniques in which the reduced resolution of the detector (usually a scintillator) is not sufficient to separate the coherent and Compton scattering peaks. In these techniques usually is used the approximation to consider the scattered photons only due to the Compton scattering. Therefore, these are employed mainly in the determination of the electron density of the tissues, using single- and dual-source configurations (refs. 1-6).

The imaging techniques using Compton scattering can be considered as belonging to this class. Attempts have been made to produce an image of internal tissue density by using an external source of gamma rays and scintillator or semiconductor detectors placed at an angle to the incident beam. Tomographic systems, using one or more scintillator scanning detectors, semiconductor detectors, and gamma camera, have been described (refs. 7-11). These were initially proposed in planning the radiation therapy and later for certain diagnostic purposes. These techniques are less precise and accurate than fixed point systems, but their capacity to produce an image is very important for many applications. Only the analytical aspects of these techniques are discussed in the present chapter.

To the other class belong those techniques that use both coherent and Compton scattering. These may be performed only with the use of high energy resolution detectors, i.e. with a FWHM of a few hundred eV, such as hyperpure Germanium detectors. The most important technique of this class uses the coherent to Compton scattering ratio, referred to here as the Rayleigh/Compton technique (R/C.T.). It was proposed about 10 years ago to measure the effective atomic number (refs. 12-14) and later to evaluate the trabecular bone mineral concentration (refs. 15-17). This technique uses the scattering intensity ratio to reduce the influence on the accuracy of the geometrical and attenuation effects.

Further, the scattering theory and the limitations of the use of these techniques "in vivo" is briefly discussed. Finally, in the last two sections the main characteristics of P.S.T. and their analytical performances are discussed.

5.2 INCOHERENT (COMPTON) AND COHERENT SCATTERING OF LOW ENERGY X- AND GAMMA MONOCHROMATIC RADIATION

In the energy range of photons of biomedical interest (i.e., in the 30 to 100 keV range), the only scattering processes to be taken into account are

(i) the incoherent (Compton) scattering and (ii) the coherent scattering, that, in this energy range is almost entirely due to Rayleigh scattering.

A better understanding of the behaviour of scattering differential cross-sections, as a function of energy (E_o), the scattering angle (ϕ) and the atomic number (Z), enables us to establish the capacity of P.S.T. to solve analytical problems. Moreover, the simple study of the cross-sections behaviour and the knowledge of the detection efficiency and the source strength, enable a first evaluation to be made regarding the possibility of carrying out a measurement.

5.2.1 Compton scattering

According to the classic theory of inelastic scattering of a photon with a free electron (using the conservation of energy and momentum), the energy of the scattered photon is related to the scattering angle by the following relation:

$$E_c = E_0\left(1 + \left(\frac{E_0}{mc^2}(1-\cos\phi)\right)\right)^{-1} \qquad (1)$$

It is well known that the energy distribution of the scattered photons is broadened around the E_c value because of the electron motion in the target (ref. 18). This broadening effect gives rise to the characteristic Compton profile: an example of this is shown in Figure 5.2, where scattering spectra produced by a monochromatic radiation (60 keV) in a low Z target detected at

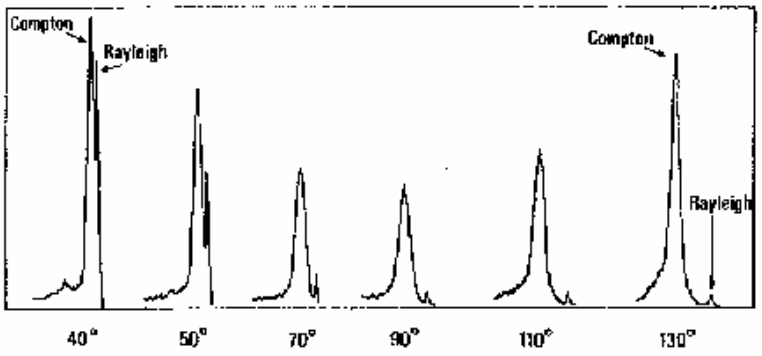

Fig. 5.2. Scattered spectrum produced in a low atomic number target by monochromatic radiation (E = 60 keV) detected at different scattering angles.

different scattering angles, are represented. This figure shows two important facts: the shift towards lower energies of the maximum of the Compton band that increases with the scattering angle and the minimum of the Compton intensity at ninety degrees.

It is worth noting that, in a configuration with finite size of the source and detector, the shape of the Compton band is partially due to geometrical effects. Figure 5.3 shows a change of the scattering angle in a sample of finite size. An imaging technique using the consequent energy shift of the Compton band maximum has been proposed by Farmer and Collins (ref. 9). This kind of effect must be taken carefully into account, especially when working with a low energy resolution detector, such as a scintillator.

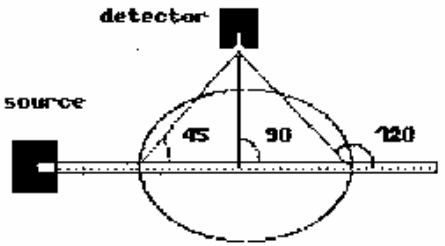

Fig. 5.3. Change of the scattering angle within a finite geometry. When the sample size is not negligible the scattering angle is not univocally defined.

An illustration of what might occur is given in Figure 5.4 showing a scattering spectrum from an ancient painting, obtained using a well collimated assembly of two americium-241 point sources and a hyperpure germanium detector. The double peak of the Compton scattering is due to the wood support behind the canvas.

Multiple scattering events also contribute to the enlargement of the Compton profile, sometimes producing characteristic small humps at the left, i.e. at lower energies of the Compton band.

The Compton scattering differential cross-section, that represents the scattering for unit solid angle ($d\Omega$) in a certain direction (see Fig. 5.1), can be expressed by

$$\frac{d\sigma_I}{d\Omega} = \frac{d\sigma_{KN}}{d\Omega} \cdot S(x,Z) \qquad (2)$$

where $d\sigma_{KN}/d\Omega$ is the Klein-Nishina cross-section for a single free electron that, using the definition of E_c given in Eq. (1), can be written as

$$\frac{d\sigma_{KN}}{d\Omega} = \frac{r^2}{2}\left(\frac{E_0}{E_c}\right)^2\left(\frac{E_0}{E_c}+\frac{E_c}{E_0}-\sin^2\theta\right) \qquad (3)$$

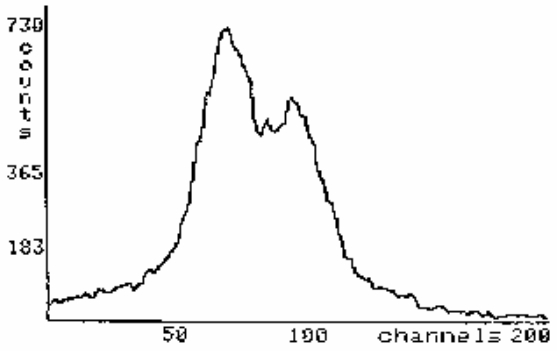

Fig. 5.4. A scattering spectrum from an old painting. The woody support behind the canvas has produced the doubling of the Compton peak.

where r is the classic electron radius (e^2/mc^2), S(x, Z) is the incoherent scattering function whose deviation from Z is a measure of the effect of electron binding, and

$$x = \frac{\sin\frac{\theta}{2}}{\lambda} = \frac{E_0}{12.4}\sin\frac{\theta}{2} \qquad (4)$$

is the momentum transfer variable. In Eq. (4), the wavelength (λ), and the energy (E_0) are expressed in Angstrom and keV, respectively.

The binding effects are important for small x values, i.e., small scattering angle and low energy, and they are stronger for high Z elements. For example for very low Z elements these effects are negligible for energy E_0 greater than 50 keV while in calcium binding effects are not negligible even for energies up to 300 keV. However, the function S(x, Z) assumes the asymptothic value of Z for high x values. A good tabulation of the S(x, Z) function has been reported by Hubbell et al. (ref. 19).

The angular distribution of the Compton scattering photons is of particular interest for some P.S.T.'s. Figure 5.5 shows the characteristic behaviour of the Compton cross-section as a function of the scattering angle at different energies E_0. It can be seen that the characteristic minimum near ninety degrees is less pronounced at lower energies, due to the electron binding effects. At higher energies and with large scattering angles, the shape of the curves is similar to that of the Klein-Nishina function. At small scattering angles, the electron binding effects are evident. At these angles, the reduced intensity of the Compton scattering is characterized by a corresponding increase in the coherent scattering (see next section).

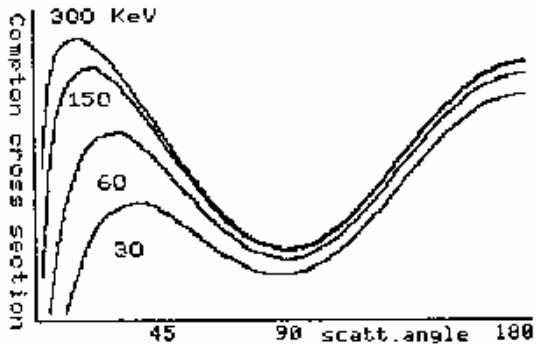

Fig. 5.5. Compton differential cross-section as function of photon scattering angle and energy. The strong reduction at very small angles (< 45 degrees) is due to the electron binding effects.

The Compton scattering intensity decreases with energy: an example of this behaviour is shown in Figure 5.6 for soft tissue. This Figure shows the characteristic decrease of the interaction cross-sections with energy; is evident the more rapid reduction of the coherent scattering and photoelectric cross-sections.

From an analytical point of view, it is more interesting the decrease of the Compton scattering intensity with Z. In particular, to study this behaviour in a multielemental target it is necessary to introduce the differential mass absorption coefficient for Compton scattering

$$\frac{\mu_1}{\rho} = N_A\left(\frac{d\sigma_{KN}}{d\Omega}\left(\sum_Z\left(w_Z\frac{S(x,Z)}{\lambda_Z}\right)\right)\right) \qquad (5)$$

where A_z and w_z are the atomic weight and the weight fraction respectively, of each element (Z) of the sample, ρ is the mass density, and N_a is the Avogadro number. The sum must be calculated upon all the elements contained in the sample.

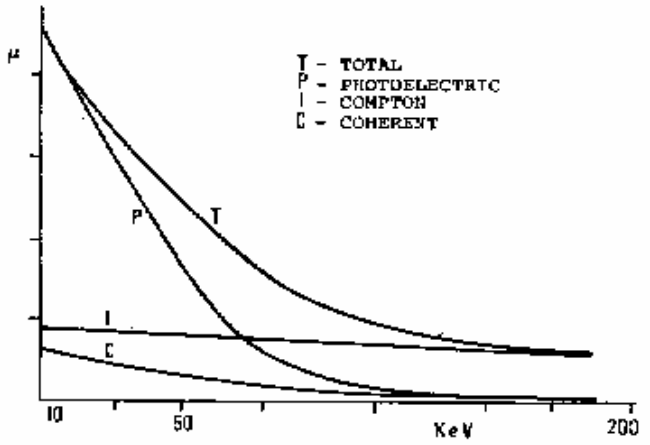

Fig. 5.6. Attenuation coefficients vs photon energy for soft tissue. The photoelectric and coherent coefficients decrease as $E^{-3.28}$ and $E^{-2.02}$, respectively.

As S(x, Z) is always lower than Z, the Compton scattering intensity decreases with Z more rapidly, than the (Z/A) ratio. In fact, for high atomic numbers, the function S(x, Z) approaches slowly its asymptotic value. This behaviour is clearly shown in Figures 5.7 and 5.8, where the Compton scattering cross-section over Z vs atomic number is reported for two energies.

However, we can expect that for high x values (i.e. energies higher than one hundred keV and not very small angles), the commonly used assumption of a direct proportionality between Compton scattering and the electron density is true. In fact, the electron density is defined as follows

$$\rho_e = \rho \sum_Z w_Z \frac{Z}{A_Z} \qquad (6)$$

where the sum is performed upon the elements compounding the material.

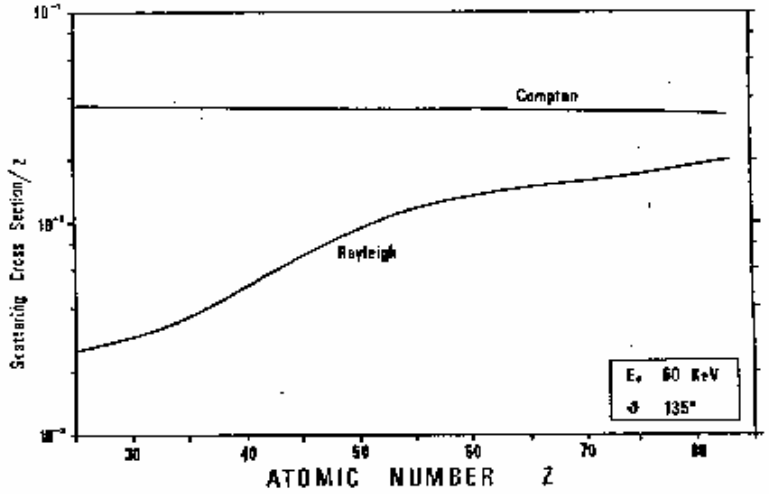

Fig. 5.7. Compton and Rayleigh scattering cross-section over Z, as a function of Z for 60 keV photons and at an angle of 135 degrees.

5.2.2 Coherent scattering

Coherent scattering, i.e. the emission in all directions of scattered photons with energy equal to that of the incident photons, is a consequence of some processes taking place in the photon interaction with bound electrons (known as Rayleigh scattering), and the nuclei (Thompson scattering). However, in the photon energy range considered here, coherent scattering is almost entirely due to Rayleigh scattering.

Coherent scattering is of increasing interest for medical physics, as recently pointed out by several authors (refs. 20-23). Much effort has been devoted, in recent years, to obtain a better theoretical evaluation of the coherent scattering cross-sections (refs. 22-24).

Coherent scattering, at first approximation, can be well explained in terms of the classic theory of the electron. When an electromagnetic wave is incident on an electron, a periodic force is exerted which sets the electron into vibration at the forcing frequency. The electron then radiates electromagnetic energy, the intensity and angular distribution of it being determined by its behaviour as an electric dipole. This radiation appears as

scattered photons of the same energy of the incident photons.

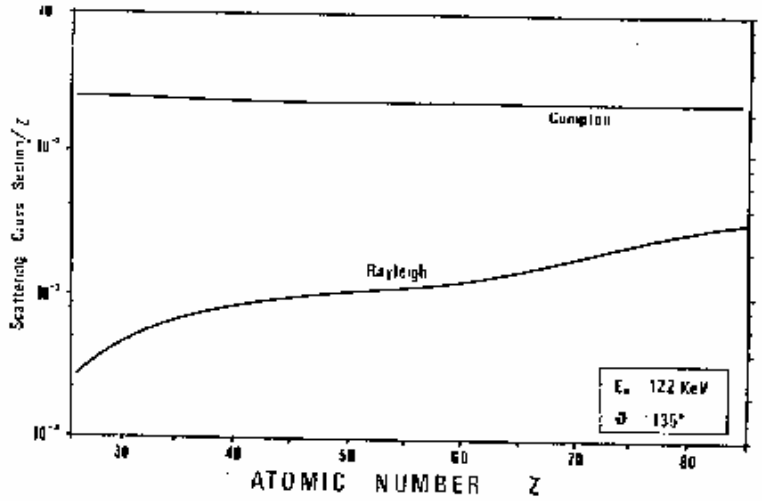

Fig. 5.8. Compton and Rayleigh scattering cross-sections over Z, as a function of Z, for 120 keV photons and at an angle of 135 degrees.

This theory seems to be in contrast with that proposed in the previous section for the Compton scattering. This is indeed true, but part of the electrons involved in the scattering processes may be considered loosely bound to their parent atoms, which in turn are bound to the crystal lattice. The theory states that the momentum of the incident photon is taken up by the parent atom, or the lattice, or the molecule. However, the coherent scattering is in competition with the incoherent scattering.

From the classic theory of the electron, it is possible to deduce the Thomson differential cross-section, given here by

$$\frac{d\sigma_T}{d\Omega} = \frac{r^2}{2}(1+\cos^2\theta) \tag{7}$$

This classic approach clearly shows how the coherent scattering strongly depends upon the primary photon polarization. In particular, the cross-section given in Eq. (7) (commonly known as Thomson cross-section) is that for unpolarized photons. According to the classic theory for polarized radiation, the

coherent scattering cross-section is null at ninety degrees. The strong dependence of coherent scattering on polarization has been recently observed in the experiments with synchrotron radiation, which is linearly polarized in the orbit plane of the accelerated electrons (ref. 25).

The dependence upon the scattering angle of the coherent scattering is strongly peaked in the forward direction, as a consequence of the process known as Rayleigh scattering. Therefore, more accurate theoretical deductions have led in the description of the coherent scattering to the introduction of a new formalism, i.e. the form factor formalism . The latter is believed to be accurate for small momentum transfer, i.e., for x values up to about 10 A^{-1} when the photon energy is large compared to the binding energy of all the atomic electrons (ref. 23).

In the form factor formalism, the coherent scattering cross-section is given by

$$\frac{d\sigma_c}{d\Omega} = \frac{d\sigma_T}{d\Omega} F^2(x,Z) \tag{8}$$

where $F^2(x, Z)$ is the atomic form factor which accounts for the wave interference of scattering from different electrons. It is useful to remember that the two scattering functions F(x, Z) and S(x, Z) are related to the atomic number by the following equation

$$Z = F^2(x,Z) + S(x,Z) \tag{9}$$

Several tabulations of the F(x, Z) factor have been reported in the literature; the most recent being that of Shaupp et al. (ref. 24).

As shown in Figure 5.6, the decrease of coherent scattering cross-section with energy is more rapid than that of the Compton scattering. Taking into consideration the relation between the momentum transfer variable and the energy, we may observe that, for a given element, the function S(x, Z) increases for increasing energies. Consequently, for Compton scattering the reduction of cross-section with the energy is due entirely to the Klein-Nishina cross-section. Conversely in the case of coherent scattering the rapid decrease of F(x, Z) function with energy determines the behaviour of coherent scattering cross-section.

To understand the behaviour of the coherent scattering cross-section with the scattering angle, analogous considerations should be made. Although, in this case we must take into account: (i) the Thompson cross-section depends on scattering angle and (ii) the relationship between x and θ is not linear. As a consequence, the reduction of the coherent scattering cross-section with the

scattering angle is very strong, as shown in Figure 5.9 where the coherent scattering cross-section is shown as a function of the scattering angle.

The most striking characteristic of coherent scattering is that it is strongly dependent upon the Z of the target. This suggested some analytical techniques to determine a higher Z element (for example calcium) in a matrix of lower Z elements.

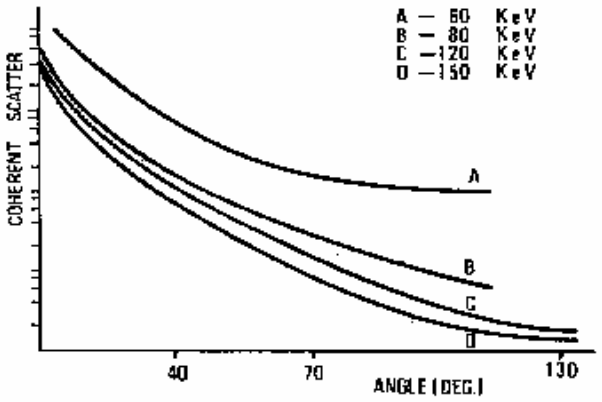

Fig. 5.9. Coherent scattering cross-section as a function of scattering angle at different energy values.

In a first theoretical approach to the coherent scattering, using a Thomas-Fermi approximation for the electron distribution, it can be deduced that the coherent scattering is proportional to about Z^3.

Later experimental and theoretical results have shown that the situation is more complex. However, the power law dependence of the coherent scattering cross-section on Z is well established.

$$\frac{d\sigma_c}{d\Omega} = K Z^n \qquad (10)$$

even if the value of the power index (n) changes markedly in the different atomic number intervals. The problem has been reviewed recently (refs. 20, 26) showing that the power index may assume values in the 1.5-7 range; in particular, it has been demonstrated that the power index becomes higher with increasing values of momentum transfer variable (x).

To have an idea of the behaviour of the coherent scattering cross-section vs the atomic number, the coherent scattering cross-section over Z, as a function of Z, is reported in Figures 5.7 and 5.8, for two energies of incident photons at 135° scattering angle. For comparison, the same relation for the Compton scattering is given. It can be seen that, in the low Z range, the coherent scattering is very strongly ($n \simeq 4$) dependent upon Z.

It is worth noting that for increasing x value (i.e., when the dependence on Z becomes stronger), the coherent scattering cross-section unfortunately quickly falls-off. This occurs in a more accentuated way for low Z elements that are of prevalent biological interest. Therefore the problem of finding the best working conditions with a technique using coherent scattering turns out to be complicated. At small angles, i.e. small x values, the intensity of elastic peak is great, but its dependence upon the atomic number is weaker and the overlapping of the Compton band with the elastic peak is stronger. At a large angle the intensity quickly decreases, but the dependence upon Z is more marked, and the overlapping problem is reduced. The question is how to find the optimal working conditions. Much efforts have been made to find criteria of general agreement (refs. 15-17, 27, 28). In the next section this problem will be discussed in relation to the R/C.T..

Finally, the increasing interest in the coherent scattering is fully justified despite the fact that the correct evaluation of the elastic peak intensity is not easy due to the marked overlap of the coherent peak with the Compton broad band. This is more evident for low scattering angles and/or low energies of incident photons (see Fig. 5.2). Some authors have pointed out marked discrepancies between the theoretical and experimental values. These occur in all cases in which a finite geometry must be used. Manninen et al. (ref. 29) have discussed the precautions that should be taken to avoid errors in the determination of the elastic peak intensity.

5.2.3 The coherent to Compton scattering ratio and the effective atomic number

The simultaneous detection of the coherent and Compton scattering intensities, which is possible with a solid state detector, has led in the last decade to the measurement of the coherent to Compton scattering intensity ratio (R/C). If one assumes that the detection efficiency and the attenuation effects are the same for the two scattered radiations (hence, they can be neglected), the R/C ratio for a given sample can be written as

$$R/C = \frac{\mu_c}{\rho} \Big/ \frac{\mu_I}{\rho} \qquad (11)$$

where μ_c/ρ is the differential mass absorption coefficient for the coherent scattering in the sample, defined in a similar manner as μ_i/ρ in Eq. (5).

As can be deduced from the two previous sections, for energies greater than fifty keV and with a quite large scattering angle (i.e., for x values not very low) the dependence of R/C upon Z is almost completely due to the coherent scattering (see Figs. 5.7 and 5.8). In Figure 5.10 the R/C ratio as a function of Z is reported, for the same values of the incident photon energies and of the scattering angle as in Figures 5.7 and 5.8. From a direct comparison of these two curves, i.e. that of the coherent scatter and that of the R/C ratio, it can be seen that their shape is very similar.

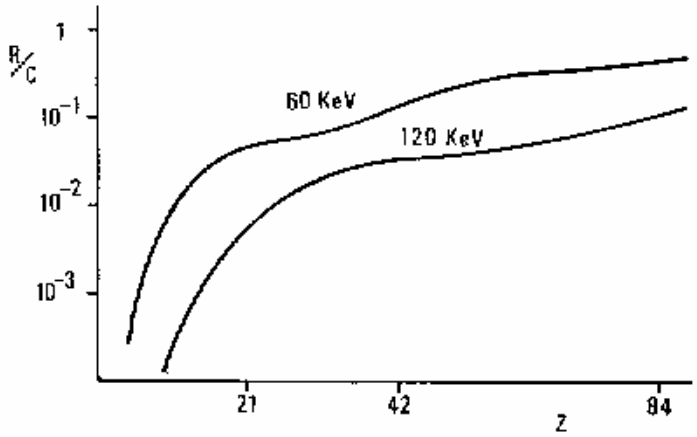

Fig. 5.10. Coherent to Compton scattering ratio R/C vs atomic number, for 60 and 120 keV photons and at 135 degrees angle.

However, for low values of the momentum transfer variable the Compton scattering also shows a stronger dependance upon Z. In these cases the approximation of the behaviour of R/C as a function of Z is complicated. Fortunately, for "in vivo" measurements (and also for field applications), where the advantages of R/C.T. are more evident, the best experimental conditions are obtained at values of x for which the Compton scattering dependence upon Z is negligible compared with the very strong dependence of the coherent scattering.

Also the behaviour of the R/C ratio as a function of the scattering

angle, is fully dominated by the coherent scattering. This is shown in Figure 5.9, where the coherent scattering cross-section as a function of scattering angle, for various energies of the incident photons are reported. It should be noted that the fall-off at increasing angles is more rapid at higher energy values.

A very interesting characteristic of the R/C ratio is its independence on the variables having the same value in both the ratio terms. In particular, this is true for (i) the density, (ii) the incident photon beam intensity and (iii) the detector efficiency and in time fluctuations of the electronic chain. The complete independence of the R/C ratio on the density, justifies the assumption that there is a direct relationship between effective atomic number (Ze) and R/C, i.e. it is possible to determine Ze directly from the R/C measurement.

The use of the effective atomic number is usually accepted. This parameter has a physical meaning and allows many characteristics of a material (or a tissue) to be visualized with a number. Unfortunately, its value depends strictly upon the technique used for its measure, i.e. for the same tissue the Ze values obtained by the use of absorptiometric and scattering techniques are not equal. Obviously, for analogous techniques an expression that relates the different Ze values for the same sample may be obtained. This problem has been well studied for dual energy X-ray transmission methods (refs. 30-32).

For transmission techniques the definition of Ze is not easy due to the different Z dependence of absorption processes such as photoelectric, coherent and Compton. In R/C.T. this definition is not even more difficult. In this case the complex energy and the Z dependence of the scattering processes must be taken into account. As shown in the previous section, the power law dependence of the coherent scatter upon Z is quite complex since the value of the power index depends upon the energy and the angle, and also upon Z. In fact, in many cases, the power law dependence for the low Z element range differs considerably from that for the high Z range.

However, many attempts have been made to find a rule to calculate Ze. Some formulas empirically deduced, have been reported in the literature (ref. 14) but their validity is limited to the experimental conditions used in that particular work. Other authors refer to a hypothetical effective atomic number without giving the rule for its calculation. More recently, Manninen and Koikkalainen (ref. 33) attempted to solve the problem for a energy of 60 keV and large angles, by assuming the coherent scattering intensity proportional to Z^3 and the Compton intensity to Z. The proposed formula is the following

$$Z_e = \left(\frac{\sum_Z w_Z Z^3}{\sum_Z w_Z Z} \right)^{\frac{1}{3}} \qquad (12)$$

They have shown that this equation gives good results for low Z materials and high scattering angles, i.e. $\Phi > 120^{\circ}$. A more general approach could be to substitute in Eq. (12) the correct n value given by the power function approximation for the energy, angle and Z range under study. Moreover, the correct dependence of Compton scattering upon Z which is not always linear could be considered. The Compton scattering dependence upon Z is weak compared to the very strong dependance for coherent scattering, especially at higher x values. Now, if we consider the dependence of Compton scattering upon Z as negligible, a possible approximated formula for the calculation of the effective atomic number could be (refs. 28, 31)

$$Z_e = \left(\sum_i w_i Z_i^n \right)^{\frac{1}{n}} \tag{13}$$

where n can be determined experimentally or calculated from the power function approximation of the theoretical R/C values.

Finally, it must be underlined that the use of the effective atomic number requires great care. In particular, for techniques using coherent scattering, a definition useful for a particular experimental situation can not be immediately generalized to other cases. In addition, it should be remembered that a Ze definition good for all Z values does not exist because of the different power law dependence of light and heavy elements. These limitations considerably restrict the use of Ze.

Apart the use of the effective atomic number, one can consider the sample under study as a two- or three-phase system. This method is extensively used in connection with the dual-photon absorptiometric, in which the bone tissue is considered as a mixture of bone mineral and soft tissue (refs. 34).

In the assessment of bone mineral with R/C.T., the bone is taken as a two phase system (ref. 15). The mineral fraction is usually referred to as Bone Mineral Density (BMD)*. The meaning of this term may be misunderstood because the R/C.T. is unable to measure directly density change.

A two-phase model may simplify the relation between weight fraction of one of the two phases and the measured R/C ratio. Under the hypothesis of small variations of the Compton scattering coefficients, Eq. (10) can be approximated with a linear relation

$$R/C = \frac{\frac{\mu_{c,A}}{\rho} w_A + \frac{\mu_{c,B}}{\rho} w_B}{\frac{\mu_{I,A}}{\rho} w_A + \frac{\mu_{I,B}}{\rho} w_B} \approx K_B w_B + K_A w_A \tag{14}$$

where w's are the weight fractions of the two components and μ_c/d's and μ_I/d's

* in the case of the trabecular bone measurements only, it becomes TBMD.

are the differential absorption coefficients for coherent and Compton scattering, respectively. In the linear approximation K_A and K_B are the coherent to Compton scattering ratios for the two components. Obviously, the sum of the two weight fractions is one in Eq. (14).

The advantage of having a linear relationship between the measured quantity and the parameter to determine is evident. In this case, in fact, it is easier to define some important figures, such as for example sensitivity and precision. As can be deduced from Eq. (14), sensitivity is given by the difference between the R/C ratio for the two components, i.e. $K_A - K_B$.

Also the statistical precision, i.e. the precision under the assumption of only statistical uncertainty, may be expressed in a very simple way

$$\Delta w = \frac{\Delta R}{K_A + K_B} = \frac{R/C}{(I_R)^{\frac{1}{2}}(K_A + K_B)} \tag{15}$$

where I_R are the total counts detected in the elastic peak.

Moreover, using the above-mentioned approximation, it is easier to answer the question concerning the choice of the best working conditions. By expressing the net signal as the product of the sensitivity and the weight fraction, and by assuming a noise due only to statistical fluctuations, it can be deduced that the signal to noise ratio can be written

$$\frac{S}{N} = (I_0 q f)^{\frac{1}{2}} \frac{\left(\frac{\mu_{c,A}}{\rho} - \frac{\mu_{c,B}}{\rho}\right) w_A}{\left(\frac{\mu_{T,A}}{\rho} w_A + \frac{\mu_{T,B}}{\rho} w_B\right)^{\frac{1}{2}}} = (I_0 q f)^{\frac{1}{2}} G(x, Z_A, Z_B) \tag{16}$$

where I_o is the intensity of the primary beam, q is the total efficiency of the measuring system and f is a correcting factor that accounts of attenuation and multiple scattering effects. If we consider a two-element mixture Z_A, Z_B, for example carbon and calcium, it is possible to study the behaviour of the S/N ratio. To do this, let us introduce the function $G(x, Z_A, Z_B)$, defined above, as a figure of merit. In Figure 5.11, a plot of $G(x, Z_A, Z_B)$ as a function of the scattering angle at several energies, is shown. It is possible to see that for a given energy the S/N ratio is high at small ($\Phi < 45$ degrees) scattering angles (where the overlapping of the two scattering peaks is greater), but it decreases rapidly reaching a fairly constant value. This ratio also decreases, at a given angle, with the energy. However, for a given energy the variations of this figure for an angle greater than seventy degree, are small. This explains the controversial results obtained experimentally by various authors. In the region of a scattering angle of about ninety degrees and for an energy of the primary beam below one hundred keV, the efficiency

and perhaps the attenuation effects play a more important role than any other variables. In fact, looking for an angle that allows a reduction of the paths inside the sample or requires a less tight collimation, one may obtain better S/N ratios at larger rather than at smaller angles.

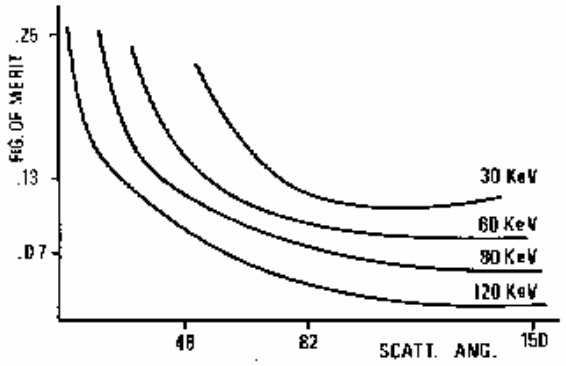

Fig. 5.11. The Figure of merit $F(x, Z_A, Z_B)$, as defined in Eq. (16), as a function of the scattering angle for several energies. The calculation has been done assuming a mixture of 25% Ca and 75% C.

5.3 THE INHERENT SOURCES OF ERROR IN PHOTON SCATTERING TECHNIQUES

In this section, problems concerning the photon scattering techniques (P.S.T.) and their use especially "in vivo", will be discussed.

One of the most attractive characteristic of the P.S.T. is the possibility to perform measurements on internal samples, i.e. samples surrounded by materials not involved in the measurement. This can be done by using suitable collimators for the source and the detector (*). As pointed out by several authors, this possibility is limited by problems affecting the accuracy of measurements (refs. 5, 15, 35, 36). Therefore, one of the major drawbacks in developing new applications of P.S.T., is the evaluation of useful correction factors to reduce the main sources of error. These may be regrouped in the following categories:

a) finite geometry effects;
b) absorption and selfabsorption effects in surrounding materials and in the sample, respectively;
c) multiple scattering effects;
d) nonhomogeneity of the sample and variability of its matrix.

The study of these effects cannot be made separatly because of the mutual influence of one kind of error upon the others. However, to understand the peculiarities of each source of errors the influence of each will be studied separately. The interconnections will be underlined in each paragraph.

(*) In the following one source and one detector geometry will be considered. Extention to multisources (or detectors) assembly can be easily done.

5.3.1 Problems arising with a finite geometry

The common statement that the measurements are always influenced by the geometrical arrangement used, is more severe for P.S.T.. In this case, it is necessary to use a source-detector set-up characterized by a finite geometry (ref. 37). Poorer efficiency of the measuring system must be carefully avoided especially for R/C.T., in which the counting rate in the coherent peak is the limiting factor. Therefore, the need to improve the measuring system response requires the use of a finite geometry.

In a finite geometry, the measured parameter is evaluated within a volume defined by the source and detector collimators. This volume is referred to as the scattering volume (s.v.). Its size and shape are defined only by geometrical factors such as the scattering angle and the distances of detector and source from the sample. Further, the s.v. depends also upon the collimator characteristics. A good knowledge of s.v. is needed in order to position this imaginary volume within the sample (i.e., in the case of "in vivo" measurement, within the studied tissue).

The s.v. may be easily visualized as the intersection volume of the two cones, the primary photon beam cone and the field of view of the detector. It has been pointed out (ref. 17) that shape and size are strongly dependent on the scattering angle. Figure 5.12 shows how a ninety degrees scattering angle produces a smaller s.v. compared with the larger (and elongated) ones at larger and smaller angles. Moreover, at ninety degrees the s.v. seems to be characterized by a more regular shape. However, the total size of the s.v. alone, is not enough to evaluate its usefulness for the measure. The system response is, in fact (see Fig. 5.13) dependent on the path lenght of incoming and outcoming photons in the sample (a and b) and in the materials surrounding the sample (c and b). For example in Figure 5.13, it can be seen how in an ellipsoidal object containing in the center a circular sample, small (forward-scattering) and very high (back-scattering) scattering angle minimize the

above mentioned distances. Obviously, in a sample not placed in the center, a back-scattering geometry is, in principle, the most convenient.

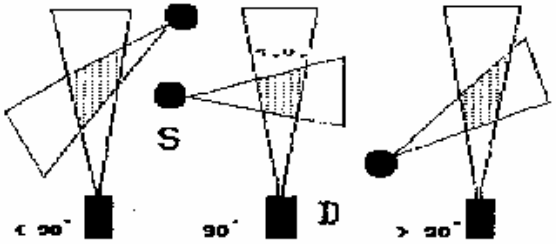

Scattering volume shape at different scattering angles

Fig. 5.12. Variations of the size of the effective scattering volume (s.v.) as a function of the angle. The size of the s.v. is smaller at an angle of ninety degrees than at larger and smaller angles.

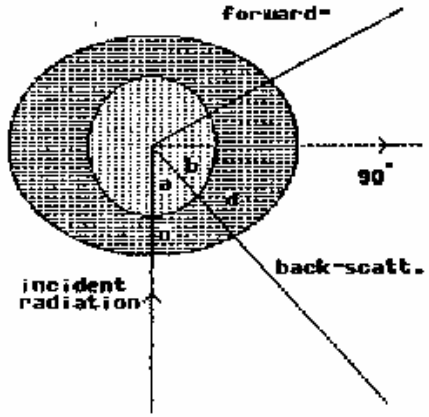

Fig. 5.13. Schematic drawing showing that with an ellipsoidal object containing in the centre a circular sample, the forward- and back-scattering geometries increase the performances of the measuring system.

In addition, it should not be forgotten that the s.v. presents an intrinsic internal non-uniformity of the response. In fact, the scattered photon

fluences coming from each elemental volume in the s.v., are not equal. For example the flow from the penumbra regions at the border of the s.v. is very small in comparison to the one coming from the central part of the s.v.. Therefore, a study of the internal structure of the s.v. must be done, i.e. the knowledge of the contribution to the detected spectrum coming from each part of s.v. because it is very useful in the evaluation of system performance and accuracy.

The experimental determination of the internal structure of the s.v. is not easy; one way is to explore it by using an object of small size, in comparison to that of the s.v.. In these measurements, a long measuring time is needed in order to obtain good counting statistics. This procedure is time consuming and unpractical. In many investigation, the evaluation of s.v. has been carried out using different size objects (refs. 5, 35, 37). This method allows one to evaluate the influence on the measuring system response of a group of effects, such as selfabsorption, multiple scattering, and finite geometry effects.

In many cases, the study of system response using objects of increasing size, is useful to validate a measuring system but is unable to give sufficient information on the internal structure of the s.v..

Recently, Wolf and Munro (ref. 38) studied how in a finite (backscattering) geometry sample positioning is critical, and there is a strong interaction between attenuation and multiple scattering effects. They have shown that the results of the measurements can also be influenced by the presence of objects outside the s.v..

The best way to study the internal structure of the s.v. is to calculate by means of numerical approximations the contributions to the detected spectrum coming from each point of the s.v.. This can be done by evaluating for each point the solid angle subtended by the source and the detector respectively, taking into account the presence of the collimator as shown in Figure 5.14. Referring to this Figure, the product of these two solid angles ($\Omega(x, y, h)$) is proportional to the fluence from an infinitesimal volume identified by the point P. The results of these calculations are profiles of the $\Omega(x, y, h)$ function in one direction or more precisely, integrals of this function along particular axes or planes as shown in Figures 5.15 and 5.16. This method allows immediate visualization of the internal structure of the s.v.. Obviously, the integral of $\Omega(x, y, h)$ on the whole s.v. gives the geometrical efficiency of the measuring system. A preliminary simulation of the s.v. structure by means of a computer, is very useful; it allows both the choice of the most favourable source-detector collimation and optimization of the performances of the system. The last point is extremely important for R/C.T.'s

where, as seen in section 5.2.3, the efficiency of the measuring system sometimes plays a fundamental role. In addition, in evaluating the accuracy of measurements on objects of variable shape and size (for instance "in vivo" measurements), knowledge of the internal structure of the s.v. is necessary. In this case the anatomy of the chosen site must be taken into account.

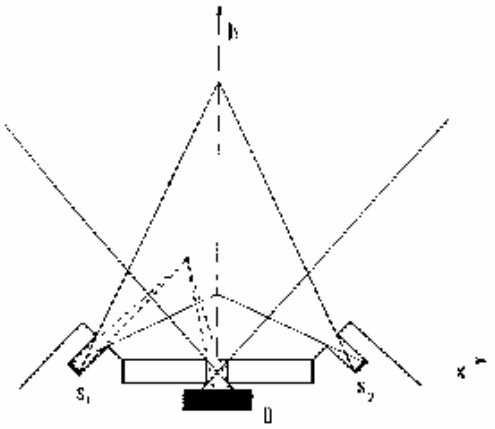

Fig. 5.14. Schematic drawing of a two-source-detector geometry. The contribution to the detected spectrum from each point of the scattering volume can be calculated by considering the solid angles subtended by the source(s) and detector.

5.3.2 Attenuation effects

There are two kinds of attenuation effects:

a) absorption of primary and scattered photons in the material surrounding the s.v.;

b) selfabsorption of the same radiation in the s.v..

The two effects behave differently. The first gives always rise to an attenuation of the signal whereas the second may determine either an increase or a decrease of the signal. To understand the nature of these two effects, let us consider the simple model depicted in Figure 5.17. In this model, a scattering layer of thickness T is surrounded by an absorbing layer H. In other words the first layer represents the s.v. whereas the second represents the surrounding materials.

Taking at first a scattering angle of more than ninety degrees, the Compton scattering intensity can be calculated integrating the absorption factors for incoming and outcoming radiation over the layer thickness (T). After the integration, regrouping the homogeneous terms, it is possible to

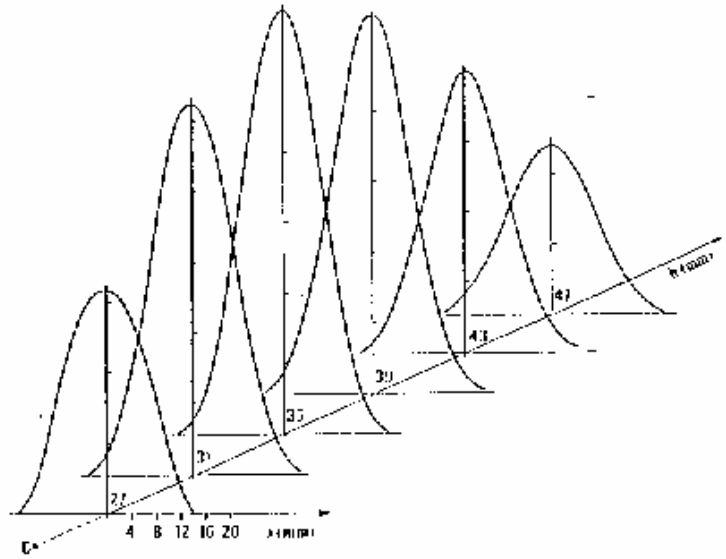

Fig. 5.15. Computer simulation of the scattering volume shape for the geometry of Figure 5.14. The profiles along the principal axes (x and h) are shown.

write the Compton scattering intensity as follows

$$I_s = \left(I_0 \frac{\mu_1}{\rho}\mu\right)\left(\frac{1}{\ldots}\cdot\frac{\exp(-kT)}{k}\cdot\ldots\right)\left(\exp(\ldots k'H)\right) \qquad (17)$$

where $k = \mu(E_c) \cdot \ldots (E_0)/\cos(\vartheta))$, $k' = \mu'(E_c) + (\mu'(E_0)/\cos(\vartheta))$ and $\mu(E)$'s and $\mu'(E)$'s are the mass absorption coefficients for the scattering and absorbing layers, respectively. In the above equation the efficiency is assumed equal to one.

The term in the second pair of brackets in Eq. (17) represents the selfabsorption contribution whereas that in the third pair, the absorption contribution. For a backscattered geometry the cosine is always negative,

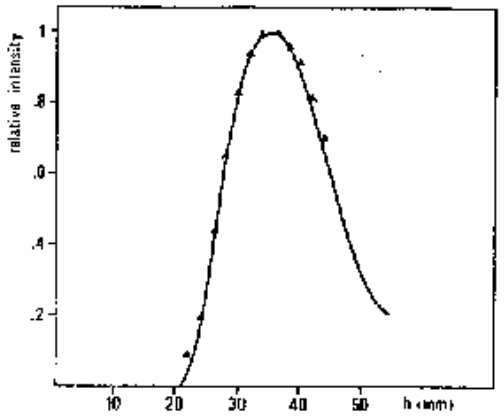

Fig. 5.16. Calculated profile along the h axis that gives in depth the system response. For comparison some experimental points, i.e. Compton scattering relative intensity, are reported. The measurements were performed with a thin sheet of absorbing material.

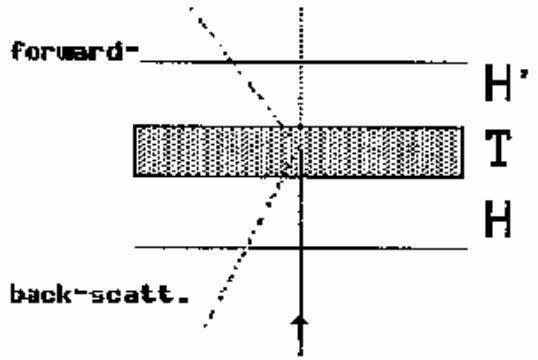

Fig. 5.17. Schmatic drawing of a scattering sample composed of three sheets. The internal sheet (T) represents the scattering volume, whereas the other two (H) represent the surrounding materials.

therefore, the selfabsorption term is always positive. For this kind of geometry, the selfabsorption always produces an increment of the detected signal. This increment becomes smaller and smaller with increasing T values. In particular, one can define a thick sample approximation, i.e. the values of T for which the increment of selfabsorption function is less than one percent. Values of thick sample approximation for bone tissue as a function of energy, are reported in Figure 5.18.

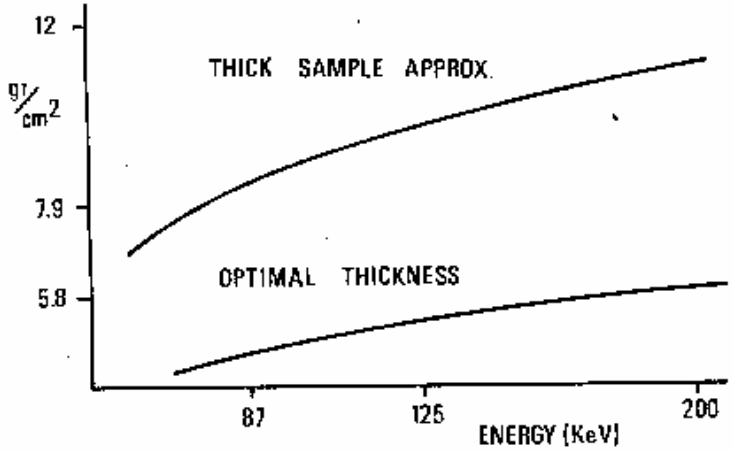

Fig. 5.18. Lower curve: optimal thickness values (Eq. (19)), for bone sample and an angle of 45 degrees, as a function of energy; upper curve: thick sample approximation in a backscattering (135 degrees) geometry (see text).

Another interesting aspect of the selfabsorption function is its behaviour at increasing Z values of the sample. In weakly absorbing samples such as biological samples, this function assumes values greater than one while in strongly absorbing samples it can be much lower than one. This explainss the drastic reduction of the backscattered radiation intensity when the primary radiation impinges on an highly absorbing object (see Fig. 5.19). Further, it must be stressed that in a two component mixture when the weight fraction of the higher Z sample component increases the detected signal becomes higher, reducing the corresponding decrease due to selfabsorption.

In the case of a scattering angle smaller than ninety degrees (forward scattering), the selfabsorption function behaviour is more complicated because the incoming photons have the same direction of the detected ones. However, also in this case it is possible to study the selfabsorption according to a

model analogous to that used in backscattered geometry as shown in Figure 5.17 where another absorbing layer of the same thickness is placed on the other side of the scattering layer. With an integration over it, it is possible to obtain a relation similar to Eq. (14) with a multiplying factor. Then the

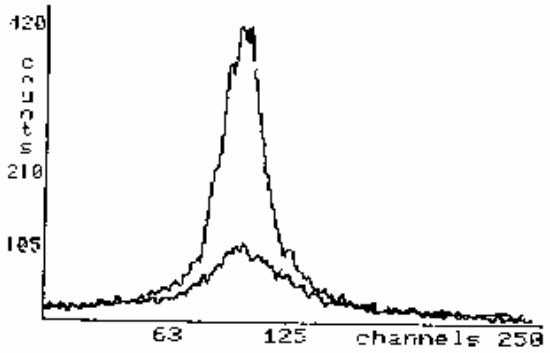

Fig. 5.19. Scatter spectra of a bone sample (upper curve) and a bronze object (lower curve)detected with the same measuring system and with equal measuring times. The marked reduction of the Compton scattering intensity in the high Z object is almost entirely due to selfabsorption.

selfabsorption term becomes:

$$G = \frac{1}{k}\cdot\frac{\exp(-kT)}{\exp\left(-\frac{\mu(E_0)}{\cos\theta}T\right)} \qquad (18)$$

where G has a maximum at:

$$T = \frac{\log\left(\frac{\mu(E_0)\cos\theta}{\mu(E_0)}\right)}{\frac{\mu(E_0)}{\cos\theta} - \mu(E_0)} \qquad (19)$$

This behaviour can be easily understood considering that the scattered intensity in a particular direction increases with T until its marginal increment (due to selfabsorption) is greater than its marginal reduction (due to the absorption). Therefore, G is symmetrical around the maximum which assumes the meaning of an optimal sample thickness. In fact, around this thickness the function is smooth, i.e. the first derivative is near zero and the detected signal is maximum. Thus, working with a sample having this optimal thickness, better precision and sensitivity will be obtained. To give an example, the optimal T values for bone tissue are reported in Figure 5.18,

as a function of the energy. It can be observed that these values are of a few grams per square centimeter (i.e., 3 ÷ 4 centimeters) for tissues while for higher Z material (for example metal alloys) are less than one millimeter. The risk of working with thicknesses greater than the optimal value is greatly reduced in "in vivo" measurements. However, if the thickness of the sample is known, it is possible to use an energy for which this value is near to the optimal.

Whilst the selfabsorption effects cannot be immediately understood, the absorption effects in the surroundings materials can be more easily explained. They give rise to an attenuation of both the incoming and the outcoming beams proportional to the absorption coefficients of the crossed materials. This relationship is clearly shown in the third term of Eq. (17). The absorption effects cannot be neglected. If one considers, for example, a bone sample localized three centimeters inside the body, the decrease in the detected signal due to the presence of the surrounding soft tissues is of sixty-nine percent at 60 keV and of sixty-three percent at one hundred keV.

Fortunately, using the ratio of two intensities the absorption effects in the material outside the s.v. can be easily corrected. Obviously, the presence of absorption cannot be completely neglected. To do this, it would be necessary to use two beams of the same energy crossing the same piece of material.

Several procedures to correct absorption in surrounding materials have been proposed for various Compton scattering techniques. These techniques and the methods used to correct the absorption of primary and scattered radiation will be described in section 5.4.

5.3.3 The problem of Multiple Scattering

In a finite size s.v. the probability that a detected photon comes from a secondary or tertiary interaction (i.e. results from two or three successive scattering events), is not negligible. Obviously, the probability of a multiple scattering event decreases rapidly with the order of the interaction. Moreover, the probability of a secondary scattering process due to two successive coherent scattering interactions is much less than that of two successive Compton scattering events or of mixed events, i.e. a coherent scattering event followed by a Compton scattering event. From these simple considerations it may be deduced that the influence of multiple scattering on the coherent peak intensity is very little (with the exception of the interactions at small angles). Therefore, the following considerations will be restricted to the multiple Compton scattering, which is by far the most probable event.

The spectral distribution of multiple scattered photons is different from that of the single scattered photons. This can be understood observing that

first order scattered photons are produced in the sample by collisions from a well-known direction, while the scattered photons of a higher order are produced in processes involving photons with complex angular distribution.

This problem is not easy to solve, and since it is highly geometry dependent, it can be treated only using crude approximations. Indeed, Kennet and Webber (ref. 35) have shown that the form of the relation between the fraction of the n-order to the first-order scattered photons which falls within a particular spectral window, and the order of multiple interaction is gaussian in nature. For the calculations they use the Klein-Nishina formula and a simple deconvolution method. They show that it is possible to find a link between the first order and the higher order spectra.

To obtain the spectral distribution of the multiple scattered photons under more realistic approximations the only way is a simulation by means of a Monte Carlo method (ref. 39). The experimental and theoretical results reported by various authors on multiple scattering spectra show that there are both an enlargement of the Compton profile and the appearance of a continuum spectrum towards lower energies. Further, the spectral distribution of the multiple scattering photons is characteristic of the particular geometry under study. In fact, it can be easily demonstrated that many effects such as attenuation and the geometry used, contribute to the spectral distribution of multiple scattering photons (see sections 5.3.1 and 5.3.2).

As pointed out by Battista et al. (ref. 10), multiple scattering plays a more important role in imaging techniques than in single point techniques. For imaging techniques, careful theoretical studies of the problem have been performed (refs. 10, 40-42); the presence of the multiple scattering strongly reduces the contrast that can be obtained. Multiple scattering is still a major problem for those techniques using low energy resolution detectors (refs. 35, 36) while becomes a minor problem in the R/C.T.'s, in which solid state detectors are used.

It is well known that the probability of a collision within a particular object is proportional to the mass per unit surface a = d l, where l is a characteristic length of the object multiplied by the mass absorption coefficient. If one wants to consider only the collision that produces a coherent or Compton scattering photon, it is necessary to multiply the above-mentioned probability by the ratio (k) of the scattering to the total absorption coefficient. As a matter of fact, if the photoelectric contribution to the total coefficient is negligible the value k is equal to about one. This happens for low Z materials and for photon energies higher than one hundred keV. In conclusion, the probability (P) of a photon being scattered in a single event is proportional to

$$p_1 \approx k\mu(E_0)a \tag{20}$$

Therefore, the probability of a photon being Compton scattered in a secondary event at a fixed angle is proportional to

$$p_2 \approx k\mu(E_0)\frac{\mu_1}{\rho}a^2 \tag{21}$$

where (μ_1/ρ) is the differential mass attenuation coefficient of Compton scattering. The probabilities of tertiary and higher order events can be similarly deduced. However, they rapidly fall-off due to the presence of a higher order power of the attenuation coefficient.

From the above two equations, it can easily be deduced that the importance of the multiple scattering is greater for big objects and for large solid angles. Moreover, if the other mechanism of interaction can be neglected the ratio of double to single scattering is directly related to the absorption coefficient (ref. 35).

The multiple scattering gives rise to an enhancement of the scattered radiation and so it behaves as an antagonist of the selfabsorption. For example, from Eq. (21) it can be deduced that in strongly absorbent media the multiple scattering contribution is more evident; however, this is not completely true. In fact, the simultaneous presence of selfabsorption strongly reduces the effective s.v. size, and consequently the probability of the multiple scattering events.

Finally, it is worth noting that multiple scattering is responsible for some curious effects described by various authors, working with objects of increasing size. They observed that the scattered radiation intensity continues to increase, also using objects of greater size than the s.v. size. This phenomenon can be explained in terms of a multiple scattering effect due to the object parts surrounding the s.v..

5.3.4 Nonhomogeneity of the sample and variability of its matrix

The use of finite size s.v. introduces in the presence of a nonhomogeneity of the sample, an additional error. The detected scattered radiation is the sum of the scattered photon fluences from each elemental volume in the s.v.. Therefore, the nonhomogeneity of the sample under study directly influences the measured quantity(-ies). It follows that the determined parameter (e.g., the electronic density, the weight fraction of a particular sample component, etc.) is a weighted mean on the s.v..

It is necessary to distinguish between the presence of a nonuniformity in

the sample, i.e. a change in the sample density and the variation of the matrix composition, for example of the amount of fat in bone tissue. These two sources of error affect the detected signal in a different way. The first affects considerably the measurements of electron density, the second affects the R/C.T. measurements of THD. Of course, these two changes may occur simultaneously.

The presence of a nonuniformity in the sample, known before the measurement, can be minimized by placing the s.v. in such a way as to reduce the amount of fluence coming from the nonuniformity region. The use of standard samples and phantoms, can make the study of the correction procedure easier.

The situation is more complex in cases of nonhomogeneities that occur casually, as shown by Coates for fractional content of air in the lung (ref. 36). The only way to treat this error is to consider it as a change of matrix composition. For example, if it is possible to measure the amount of air in the lung, this error can be corrected taking into account the decrease in the scattered radiation with increasing air content. Generally, the correction of the measured intensity both scattered and transmitted, can be expressed as a linear function of the change of matrix composition.

The variability of the sample matrix is a source of error almost ever present in the P.S.T.'s. The method to correct this kind of error is to consider the sample as a ternary mixture. In particular, one component represents the parameter under study while the other two simulate the matrix. An example of this model is bone tissue (refs. 17, 43), which can be considered as a mixture of bone mineral (hydroxiapatite), soft tissue, and fat (the last two components can simulate the non mineralized matrix of the bone). The problem is to foresee the amount of fat in the bone; actually, this cannot be easily done. The study of the behaviour of the scattered radiation intensity with increasing fat content can provide only an estimation of the accuracy error.

The intensity ratio at two different energies is often used to correct absorption in materials surrounding the s.v.. This method is also used to correct variations of sample matrix. Obviously, the best correction is when the two intensities are simultaneously recorded with the same detector. This is always true for R/C.T. while for Compton scattering techniques the situation must be considered for each individual case.

The sample matrix variability changes the effective value of the atomic number and/or electron density of the sample simulating a variation of the component under study. This reveals another ambiguity in the use of effective parameters such as Z_{eff}.

5.4 COMPTON SCATTERING TECHNIQUES

Several Compton scattering methods have been proposed using Compton scattered radiation (or scattered and transmitted radiation), to measure the electron density within a particular internal part of the object. Medical applications of these methods have been reported in two main areas: a) bone and lung densitometry (refs. 1-6, 44, 45), and b) whole body tomographic imaging (refs. 7-11). These techniques can be subdivided into three groups a) dual and single energy Compton scattering densitometry (refs. 1-2); b) dual energy Compton scattering densitometry, using only scattered radiation according to a method proposed by Hoddleston and Weaver (ref. 6); c) Compton scattering imaging (refs. 7-11).

These methods will be described in the next three sections and the principal results obtained will also be reported.

Another analytical use of the Compton scattered radiation concerns the measurement of sample mass. This application is based upon the relationship existing between the intensity of the Compton scattered radiation and the sample mass involved in the scattering processes (ref. 46). Obviously, the Compton scattered intensity is also a function of the sample composition. This is a very strong limitation for samples of variable composition at small values of momentum transfer (see par. 5.2.1), especially for high Z materials. So far, this measurement is used only for correcting sample mass variations in energy dispersive X-ray fluorescence techniques (XRF).

5.4.1 Techniques using the transmitted and Compton scattered photons

In the early seventies two different Canadian groups described the basic method for Compton densitometry and used transmitted radiation to correct the attenuation effects (refs. 1-2). In this method a single or dual source configuration can be used according to the primary photon energies and scattering angle.

The simple idea on which these methods are based, is that of measuring the attenuation of the primary and scattered beams, through transmission measurements using sources of appropriate energy (see Fig. 20). In particular, the Compton scattered photons in a given direction have an energy distribution around the value given in Eq. (1) (see par. 5.2.1). Therefore, by using a second source having this lower energy, one can correct for the attenuation of the Compton scattered beam. A set of matched pairs of low energy monoenergetic gamma sources may be proposed for this kind of measurement.

The basic idea is to perform two scattering measurements by rotating the sample of an angle of 180 degrees and simultaneously two transmission measurements, using a second detector. The paths in the transmission and scattered

measurements are the same. In this method, the sample should be of very small size. The four equations for attenuation and scattered processes are given as follows:

$$
\begin{aligned}
S_1 &= I_1 \frac{\mu_1}{\rho} \rho C_a \exp\left(\mu(E_0)e\right) \exp\left(\mu(E_c)h\right) \\
S_2 &= I_1 \frac{\mu_1}{\rho} \rho C_a \exp\left(\mu(E_0)g\right) \exp\left(\mu(E_c)f\right) \\
T_1 &= I_1 \rho C_b \exp\left(\mu(E_0)(e+g)\right) \\
T_2 &= I_2 \rho C_a \exp\left(\mu(E_c)(f+h)\right)
\end{aligned}
\tag{22}
$$

where C_a, C_b are the detector efficiencies at the two energies E_a and E_c, respectively.

Now, dividing the product of the two scattered intensities (S_1, S_2) to that of the two transmitted (T_1, T_2) ones, we obtain

$$
\rho_e \propto \rho \frac{\mu_1}{\rho} \cdot \left(\frac{C_b I_2}{C_a I_1} \frac{S_1 S_2}{T_1 T_2}\right)^{\frac{1}{2}} \tag{23}
$$

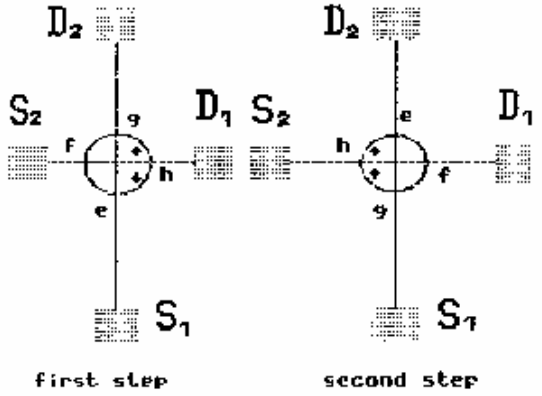

Fig. 5.20. Schematic drawing of the sources (S_1, S_2) and detectors (D_1, D_2) for electron density measurements using both transmitted and scattered photons.

From Eqs. (5) and (22) it can be deduced that the electron density is proportional to the ratio of the scattered to the transmitted intensities. Therefore, this method can be used to determine the electron density of the

sample but not its density. The latter can be deduced knowing the value of the effective (Z/A) ratio (see below) of the sample under study.

It is worth noting that at the energy and scattering angle used in these techniques only a proportionality relation between the electron density and Compton scattering intensity can be obtained. The proportionality constant is determined by performing the same set of measurements on a water sample. This step only partly resolves the problem. In fact, the influence due to the different elemental composition of the standard sample, i.e. water, and the unknown sample, for example bone sample, still remains.

Another severe limitation of the described method is the assumption that the effective path lengths of a transmitted and a scattered beam in the sample are the same. As clearly shown in Figure 5.21, the dimension of the transmitted photon beam is only determined by the collimator of the detector used while the shape of the scattered photon beam is defined by the combination of both source and detector collimators.

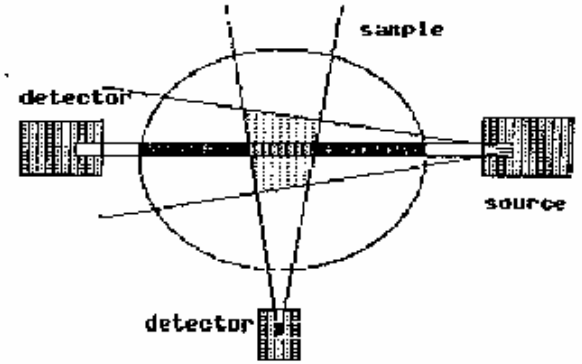

Fig. 5.21. Plan view of the measuring system showing the geometry of scattered and transmitted beams. The average attenuation for the scattered beam is less than that for the transmitted beam.

The assumption that the sample size is very small implies that the selfabsorption effects can be neglected. Good results are thus obtained only for small variations of the sample size. Huddleston and Bhadori (ref. 5) have shown that measurements with this photon scattering technique are strongly dependent on the sample size. They have attributed the observed bias in the electron density determination to the concomitant action of the multiple

scattering and the selfabsorption effects.

Many changes in the original method have been proposed by various authors, in particular, Olkkonen and Karjalainen (ref. 4) described a single-source low energy, small scattering angle, method; this method has later been extensively used by Huddleston (refs. 5, 37). Webber and Coates (ref. 45) constructed a three source densitometer for measurement of lung density. This system avoids the rotation of the object under study.

In their original work Garnett et al. (ref. 2) demonstrated how the use of an energy close to ninety keV improves the overall performances of a Compton scattering technique for the measurement of bone density. To reach this conclusion they studied the energy behaviour of: a) the Compton scattering differential mass absorption coefficient; b) the total mass absorption coefficient of soft tissue and bone; c) the detector efficiency and d) the time required in order to attain a given dose from a fixed source strength.

It is well known that Compton scattered radiation decreases with increasing energy, just as the absorption coefficient and the detector efficiency; the smaller attenuation of the beams with increasing energy, is fully compensated by the simultaneous reduction of detector efficiency and Compton scattering intensity. Then, the optimum energy can be found looking at the energy dependence of the Compton scattering intensity for unit dose; this curve has a maximum at about ninety keV.

Apart from the first system proposed by Clarke (ref. 1) using a pair of high energy sources, almost all the single point Compton scattering systems work with radioisotopic sources with an energy in the 80-130 keV range. Preuss et al. (ref. 47) studied the problem of the monochromatic sources available for these measurements. They give a list of possible pairs of sources and the corresponding scattering angle to be used. Table 5.1 shows the most interesting sources available for single and dual source techniques.

TABLE 5.1

Sources available for single and dual source techniques.

Isotope	energy (keV)	half life	second source	angle (degrees)
Ba-133	80 (36%)	8.9 y		
Tm-170	84 (3.3%)	129 d	Ba-133	44
Gd-153	99 (5%)	239 d	Tm-170	86
Eu-155	87(32%),105(20%)	1.8 y		
Co-57	122 (87%)	269 d	Gd-153	86
Se-75	134 (57%)	122 d	Co-57	51
Ce-144	134 (11%)	282 d	Co-57	51

The analytical performances of P.S.T.'s both in laboratory and "in vivo" measurements are well established. In the assessment of bone density, Webber and Kennett (ref. 3) found that with 3-minute measuring time it is possible to obtain a statistical precision of 1%. Moreover, assessing the overall precision they found values of 1.5%. Finally, they studied the accuracy of the technique in relation to the major sources of error, i.e. finite geometry, non-identical geometry, and multiple scattering. After a careful study, they found that the bias in the measurements is usually positive and that the accuracy is of 10%.

Huddleston et al. (refs. 5, 37), using the Compton scattering densitometry studied how the relative electron density is strongly influenced by both the density and the size of the sample. They used cylindrical samples with a diameter in the range 4-8 cm filled with compounds having a density range of 0.9-1.8 g/cm^3. They found that the positive bias is particularly evident in the larger samples filled with compounds of higher density. Furthermore, they found variations in the measured electron densities in the range between 2-9% and observed that the density bias increased for higher density and for greater samples. These authors showed that corrections can be introduced using a linear approximation (ref. 37).

Shrimpton (ref. 48) studied the analytical performances of these methods in the determination of the electron density of different low Z liquids. Performing "in vitro" measurements on thirteen different liquids, he demonstrated that a very good linear correlation can be achieved between measured and theoretical electron density values (see Fig. 5.22). This result clearly reveals the analytical capabilities of this method. Similar conclusions can be attained from the results reported by Huddleston et al. (refs. 5, 37).

Shrimpton (ref. 48) evaluated the performances of these methods in measurements on the electron density of human tissues. The results obtained (see Table 5.2) are very encouraging as far as the tissue characterization is concerned. The precision exceeded 1.5% for laboratory measurements, while for "in vivo" measurements the situation is more critical, for the reasons already mentioned.

It is particularly interesting to determine of the effective ratio (Z/A) of materials as discussed by various authors (refs. 5, 48). From the definition of the electron density (see Eq. (6)) it is possible to deduce the density of a given material knowing only the effective (Z/A) ratio defined as below

$$\left(\frac{Z}{A}\right)_{eff} = \sum_Z w_Z \frac{Z}{A_Z} \qquad (24)$$

Unfortunately, the value of $(Z/A)_{eff}$ cannot be measured independently but only deduced from the composition of the sample. The $(Z/A)_{eff}$ must be determined before the measurements if the goal of them is to determine the sample

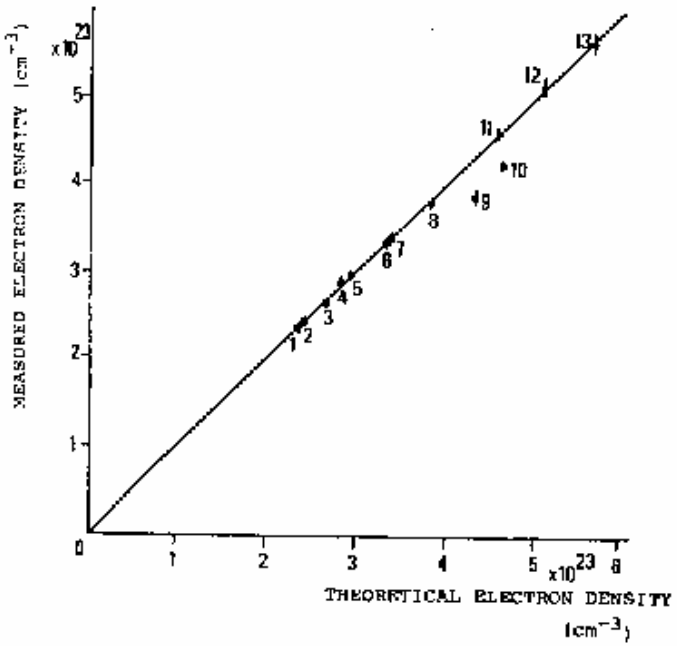

Fig. 5.22. Comparative plot of measured vs calculated electron density for the following liquid samples: 1) n-heptane, 2) Diethyl ether, 3) Isopropyl alcohol, 4) Xylene, 5) Ethyl acetate, 6) Water, 7) Glacial acetic acid, 8) Formic acid, 9) Chloroform, 10) Carbon tetrachloride, 11) Fuming nitric acid, 12) Perchloric acid, 13) Conc. sulphuric acid. (after Shrimpton, ref. 48).

density.

One of the uses of the methods described in the present paragraph is the "in vivo" determination of lung density. The wide range of values for lung density, 0.26-1.06 g/cm^3, encourages this application. These density variations are only in part to be attributed to the state of the lung. However, Webber and Costas (refs. 36, 45) using a three sources densitometer optimized for this application, have obtained good results in terms of statistical precision (2.2%), total precision (≅ 5%), and accuracy. The accuracy of the

method has been extensively studied by these authors using wood phantoms. They conclude that no relevant contribution is to be expected from the effects discussed in section 5.3.3 with the exception of the influence on the measurement of the value of the fractional air content of the lung. The only way to reduce the influence of this effect is to perform measurements at fixed lung volume. In this case the accuracy error turns out to be acceptable.

TABLE 5.2

Calculated and measured electron densities of some selected tissues.

Sample	density g/cm^3	elect.density range* (calculated)	elect.density* (measured)
Adipose tiss.	0.92-0.93	3.08-3.13	3.10 + 0.02
Brain	1.03-1.04	3.41-3.47	3.47 + 0.03
Breast	0.97-1.05	3.21-3.46	3.40 + 0.03
Kidney	1.05	3.41-3.48	3.43 + 0.05
Liver	1.05-1.07	3.49-3.57	3.50 + 0.05
Lung	0.26-1.06	0.86-3.48	2.29 + 0.03
Muscle	1.04-1.06	3.41-3.50	3.51 + 0.04
Pancreas	1.02-1.05	3.38-3.51	3.48 + 0.02
Spleen	1.05-1.06	3.47-3.52	3.46 + 0.02
Thyroid	1.04-1.07	3.45-3.55	3.61 + 0.04

* $\rho \times 10^{23}$ (e/cm^3)

5.4.2 Dual-energy Compton scattering method

Huddleston and Weaver (ref. 6) recently introduced a new Compton scattering method using a dichromatic source. This method has the advantage of avoiding the rotation of detectors and sources around the sample under examination.

A schematic drawing describing the dual-energy Compton scattering method, is shown in Figure 5.23 which also defines some of the symbols used below. This method starts with the assumption that the measuring system involves a s.v. small compared to the sample size. It is to be noted that the Compton scattering intensity produced in samples of increasing size decreases with the increasing of the sample size. This phenomenon is due to the absorption of both the primary and scattered photons by the sample parts not involved in the scattering processes. In this case, if there is further material surrounding the sample, the scattering intensity decreases exponentially with the increasing of the path lengths of the two beams in the sample and in the surrounding material. If we now introduce the two total path lengths for the sample s_s and for the external materials s_E and correspondingly define the effective attenuation coefficients k_s and $k_E(E)$, the Compton scattering intensity for a given

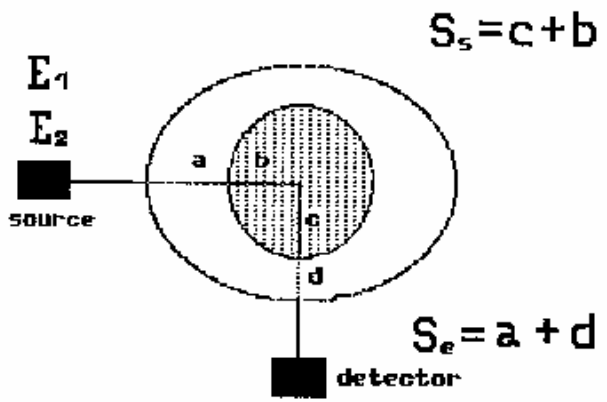

Fig. 5.23. Schematic drawing of the geometry of the source-detector system in dual-energy Compton densitometry.

energy of the primary beam, may be written as

$$S_1 = K_1\rho_e \exp\left(-k_S(E_1)S_S\right)\exp\left(-k_E(E_1)S_E\right) \qquad (25)$$

where $K_1\rho_e = I_0 C_1 \frac{P_1}{\rho}\rho$

Provided that the total path length $D = S_s + S_e$ may be estimated and the effective attenuation coefficients may be independently determined, a system of three equations and three unknowns may be written

$$\begin{aligned} S_1 &= K_1\rho_e \exp\left(-k_S(E_1)S_S\right)\exp\left(-k_E(E_1)S_E\right) \\ S_2 &= K_2\rho_e \exp\left(-k_S(E_2)S_S\right)\exp\left(-k_E(E_2)S_E\right) \\ D &= S_S + S_E \end{aligned} \qquad (26)$$

where the two scattering intensity relations concern two different energies. In this method it is necessary to simultaneously detect the two scattering intensities, using the same detector.

Resolving the system of Eqs.(26) for ρ_e one finds the following Equations

$$\rho_e = \frac{S_1}{K_1}\exp\left(k_S(E_1)S_S\right) + \left(k_E(E_1)(D - S_S)\right)$$

$$S_S = \frac{J_E D - \ln\frac{S_2 K_1}{S_1 K_2}}{J_E - J_S} \qquad (27)$$

$$J_E = k_E(E_2) \quad k_E(E_1)$$

$$J_S = k_S(E_2) - k_S(E_1)$$

The effective attenuation coefficients may be evaluated using samples of increasing size and known composition; during these measurements no surrounding substance should be used. The coefficients at each energy are determined by curve-fitting of $\log s$ vs. S_b (see Eq. (25)) according to Huddleston and Weaver (ref. 6). From a direct comparison of measured and theoretical attenuation coefficients concerning substances of known composition, it was possible to validate the efficacy of the method.

From the few results published so far, the characteristics of this method seem very promising. In the first paper by Huddleston and Weaver (ref. 6) a table comparing the theoretical and measured electron densities of different materials is reported. Their apparatus was equipped with a gadolinium-153 sealed source and a scintillator, both tightly collimated in a 90 degree geometry. The estimated precision always exceeded 3% and the accuracy, evaluated by direct comparison of theoretical and experimental values, exceeded 3.5%.

In a later investigation, Huddleston and Sackler (ref. 49) used iridium-192 source (emitting 317 and 468 keV photons) in order to obtain a better separation between the two scattered peaks, detected simultaneously by a scintillator detector. Also in this case, a ninety degree scattering angle was used. The results obtained in both the two works are very encouraging as shown in Table 5.3. The precision exceeds 2% and the accuracy 4%.

TABLE 5.3
Calculated and measured electron densities of some substances.

Substance	density g/cm^3	elect.density* (calculated)	elect.density* (measured)	% diff.
H_2O	1.00	3.344	3.233	-0.63
NaCl	1.013	3.032	3.044	+0.40
KBr	1.133	3.188	3.249	+1.91
$CaSO_4$	1.183	3.647	3.711	+1.75
K_2HPO_4	1.458	4.386	4.381	-0.11
K_2HPO_4	1.699	5.110	5.081	-0.57

* $\rho \times 10^{23}$ (e/cm^3)

The use of higher energy photons reduces the influence of some major sources of error, such as multiple scattering, finite geometry, and attenuation, and qualifies this new method as a valid alternative to that described in section 5.4.1. In addition, this method is promising for in "in vivo" measurements in relation to radiotherapy treatment planning and skeletal bone densitometry, provided that a very small s.v. can be used.

5.4.3 Imaging Techniques using Compton Scattering

The measurement of the photons fluence which a small volume of a sample scatters by Compton effect from a narrow incident beam of monoenergetic X- or gamma-radiation, provides a direct method for determining the electron density of a volume inside the sample. This simple principle in conjunction with various imaging techniques, has been used to image transverse and longitudinal sections of the body. In particular, the imaging techniques so far proposed are able to reconstruct an internal section: (i) transversal using point-by-point imaging (refs. 7, 8, 10) or line-by-line imaging (ref. 9), or (ii) longitudinal using a planar beam of gamma-radiation and a gamma-camera (ref. 11).

In this subsection the main characteristics of these techniques are briefly outlined, the aim being to allow the reader to make an initial comparison between the analytical capacity of single point and imaging techniques.

Compton tomography was developed initially by Lale (ref. 7) using a narrow photon beam (3 mm diameter) which passed through the patient. In this system, the rays scattered from a small volume of tissue are accepted by a large focusing collimator behind the patient and reach a scintillator. The direct beam and the rays scattered by the tissues surrounding the small volume are absorbed by this collimator. By scanning both the beam and the detector along the patient, the Compton scattering intensities can be used for constructing an electron density image.

Lale initially used an Iridium-192 source emitting photons in the energy range 300-600 keV, and later X-rays from a linear accelerator (5.6 MeV X-rays). The results obtained by Lale were not completely satisfactory either in the spatial resolutions (1 cm) or in tissue electron density resolution (5%). Modifications of the Lale tomograph have been described by Clarke et al. (ref. 8) who used cobalt-60 and caesium-137 sources.

The technique used by Lale (see Fig. 5.24) consists in a large detector and a multi-hole collimator for recording possibly only the singly scattered radiation from a small volume. The size of s.v. limited the obtainable spatial resolution.

Conversely, Farmer and Collins (ref. 9) used a completely different

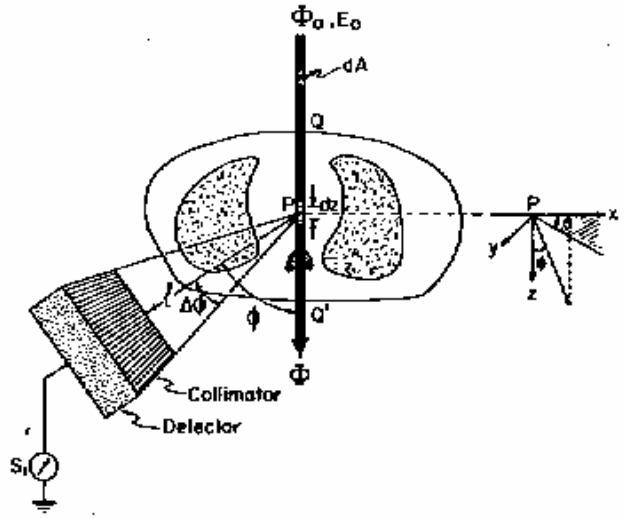

Fig. 5.24. Basic principles of tomography with Compton scattered radiation using a multihole collimator and a single scintillator detector. (after Battista and Bronskill, ref. 41).

strategy, recording with a small detector the scattered photons form all parts of the primary beam (see Fig. 5.25). The energy of the Compton scattered photons determines the interaction point along the primary beam. In this technique a highly monoenergetic primary beam is needed as well as a detector with very good energy resolution, i.e. a solid state detector. In other words in the Farmer and Collins' method the spatial resolution along a line is limited by the detector resolution. The relationship between the energy shift and the scattering angle is non linear, so the length of the segment usefully recorded in a single measurement must be negligible. Since the energy shift increases with increasing photon energy, in this technique it is advisable to use high energy radiation (compatible with the reduction of the detector efficiency). Until now, this technique even if very interesting has not produced good quality analytical results.

Later, Battista and al. (refs. 10, 41) developed several new methods to correct for multiple scattering and attenuation. They built a Compton scanner characterized by a caesium-137 source and a scintillator detector; the system was later used "in vivo" with satisfactory results. Battista and Bronskill (ref. 50) employed the Compton tomography as an aid for planning radiotherapy.

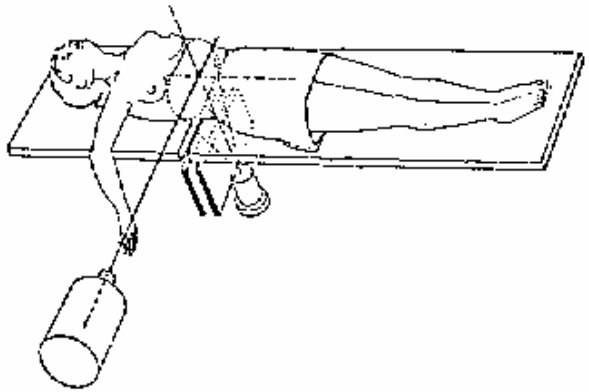

Fig. 5.25. The tomographic system proposed by Farmer and Collins (ref. 9) using a germanium detector.

To this aim, they made a thorough analysis of the analytical performances of their device; results of a direct comparison of Compton-measured and true electron density are reported in Figure 5.26. Linear regression analysis shows that the maximum deviation from linearity is 0.038, in terms of relative electron density. Moreover, Battista and Brooskill compared the results that can be obtained by using Compton and CT scanners. They concluded that the Compton scattering technique is able to image transverse sections with a spatial resolution of 0.5 cm and a relative electron density accuracy of 4% at a maximum radiation dose for the patient of 11 rad. They stressed that this standard of performance approaches the theoretical optimum for Compton imaging but falls short of the capability of commercial X-ray CT scanners. The only advantages of the Compton technique are the more easily imaging of the patient under radiotherapy treatment and measurement of the direct electron density distribution.

The imaging technique developed by Guzzardi et al. (refs. 11, 51) uses a collimated fan beam of monochromatic gamma rays produced by a linear source of mercury-203 (279 keV gamma rays) and a gamma camera placed at 90°, equipped with a parallel hole collimator (see Fig. 5.27). This technique allows an ideal tomography insofar the image plane (slab) is irradiated. The dose necessary for a single measurement is lower than that required by analogous techniques. Guzzardi et al. (ref. 11) used this technique to visualize density

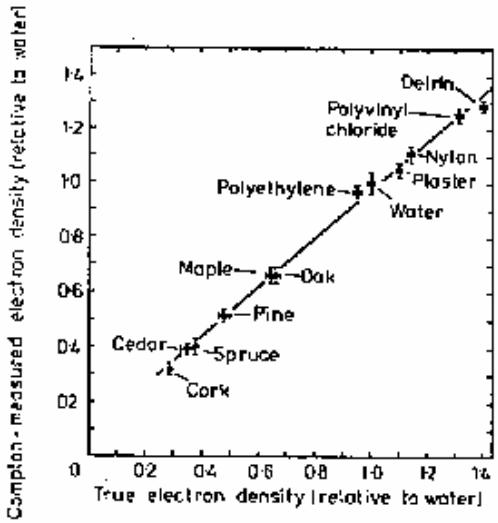

Fig. 5.26. Calibration of the Compton scanner designed by Battista and Brooskill (ref. 50) in terms of electron density relative to water. The average deviation from linearity (full line) is 0.015, and the maximum deviation is 0.038.

gradients in the chest; in lung pathology marked changes in density (see Table 5.2) have been observed by the authors. They pointed out that due to the attenuation and multiple scattering effects, results are limited. In experimental evalution, a 14% precision in the determination of electron density was reached without correcting attenuation.

In conclusion the imaging techniques, despite the fact that they offer a tomographic image, are characterized by limited analytical performances compared to the single point techniques. The use of more efficient correction methods for attenuation and multiple scattering effects, would only partially compensate this disadvantage. Furthermore, there is strong competition between these and the CT techniques. Recently, a mixed system that used transmitted and Compton backscattered radiation has been proposed by Brateman et al. (ref. 42); results show that complementary information can be obtained from the Compton scattering and CT images. Moreover, Harding and Fischler (ref. 52) have developed a new tomographic system in which a high intensity X-ray tube (160 kVp, 3 kW) and two multidetector arrays (sixty-four BGO detectors). The

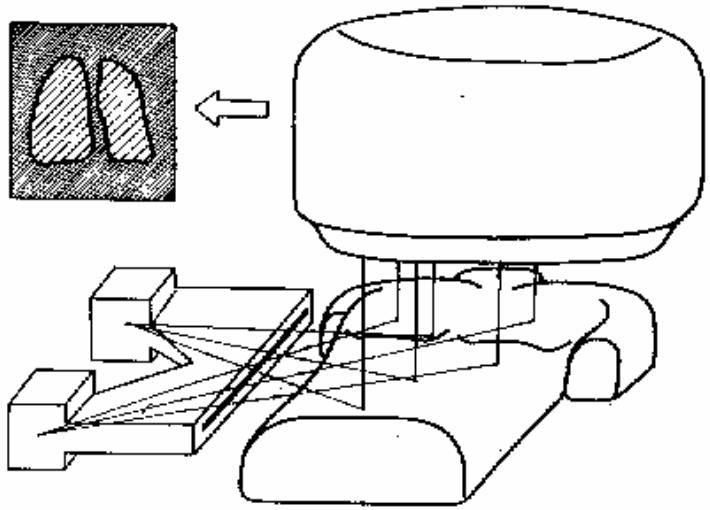

Fig. 5.27. Schematic illustration of 90 degrees Compton tomography of the lung with the technique proposed by Gazzardi et al. (ref. 11).

analytical performances of this system, using a dual energy method, have been assessed with a phantom finding encouranging results. Probably, in the near future, following these new proposals we might expect to see CT systems endowed with additional detectors in order to record scattered radiation; these new systems could produce two complementary images.

5.5 THE COHERENT (RAYLEIGH) TO COMPTON SCATTERING RATIO TECHNIQUE (R/C.T.).

The first proposal to use the ratio of the two scattered peak intensities was made by Kunzendorf in 1972 (ref. 12). This first work immediately showed the potentialities of the method despite the primitive (uncollimated) set-up used. Kunzendorf results were obtained with a backscattering geometry, using a Si(Li) detector (FWHM=250 eV) and plutonium-238 (emitting 13.5, 17.2 and 20.2 keV photons), cadmium-109 (22.1 and 24.9 keV) and americium-241 (59.4 keV) radioisotopic sources. The results reported demonstrated that the value of the power index of the R/C ratio vs Z relation was greater for higher energies of

primary photons.

Later, Puumalainen et al. (ref. 13) started extensive studies on this method; they proposed the use of the R/C ratio in the measurement of TBMD using an americium-241 source and a ninety degrees scattering angle. The coherent to Compton scattering ratio technique became more interesting with the introduction of solid state detectors and in particular of planar germanium detectors, which have a very good energy resolution (FWHM 200-400 eV) and a high counting efficiency also in the hundred keV ranges. With this type of detector it is possible to resolve the elastic peak from the Compton band. Clearly the counters used are solid state detectors.

In 1979 Schätzler (ref. 14) described the first analytical applications of the R/C.T. using an americium-241 source and scattering angles of 48 and 68 degrees. Analysing twenty-six organic compounds, he found a relationship between the R/C ratios and an empirically defined effective parameter, the effective atomic number; his aim was to demonstrate that it is possible to identify a compound only by measuring its R/C ratio. Figure 5.28 shows the plot of the R/C ratios relative to water as a function of the effective atomic number. Schätzler approximated these values with a power function of Z, introducing an index of 3.5 which agrees with the strong dependence of coherent scattering coefficient on Z discussed in section 5.2.2. This author also

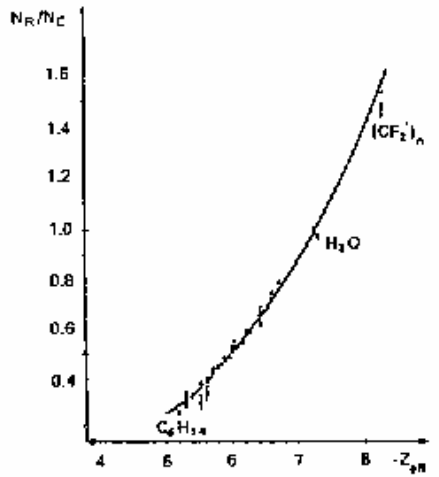

Fig. 5.28. The coherent to Compton scattering ratios relative to water, for 26 organic compounds. The primary beam energy was 60 keV and the scattering angle 68 degrees. (after Schätzler, ref. 14).

also gave examples of the analysis of binary mixtures; he attempted to determine the percentage of fat content in milk and in meat using R/C.T.. From the results reported, it can be seen that a precision of 3.4 % can be reached with a measuring time of a few hundred seconds. Similar results have been obtained by Punmalainen et al. (ref. 53) in the determinations of iodine in tissues. The results reported showed a precision of about one milligram per cubic centimetre. It can be observed that the typical sensitivity of the R/C.T. in measurements of concentration of a particular element in a sample, is very low as compared with that of other analytical techniques such as X-ray fluorescence and neutron activation analysis. These latter two techniques can be also employed in "in vivo" measurements. The above-mentioned results in the very early attepts already, characterized R/C.T. as an analytic technique able to perform bulk analysis rather than the determination of a single element present in a sample at low concentrations.

Almost simultaneously in the 1980's some groups proposed the use of R/C.T. to the determination of TBMD, using a small scattering angle and energies around one hundred keV (refs. 15, 16). In particular, Stalp and Mazess (ref. 16) carried out experimental studies on the behaviour of the R/C ratio using radioisotopic sources of americium-241 and gadolinium-153 and a scattering angle of less than sixty degrees. Their conclusions were that with a 103 keV energy of the primary beam and at a scattering angle of thirty degrees (i.e. at a value of momentum transfer variable of 2.15 A) better results can be obtained than at ninety degrees using an americium-241 source ($x = 3.42$). Stalp's conclusions can be explained considering that at 103 keV with a scattering angle of 30 degrees there is both a lower x value and a lower attenuation of the primary and scattered beam. However, it should be pointed out that in this work the authors did not attempt to optimise the geometry at different angles but used the same collimation condition at 30 and 60 degrees. No larger scattering angle was investigated.

Kerr et al. (ref. 15) using a very tightly collimated experimental set-up introduced a procedure to optimise the performance of the measuring system with respect to primary beam energy and scattering angle. Using this procedure they found that the best conditions are attained at an energy of 80 keV and a scattering angle of 25 degrees. The procedure was as follows. For a given energy and scattering angle, the FWHM of the Compton band was determined by assuming a given spread of the scattering angle and introducing the detector resolution. The coherent peak and the Compton band are considered to be resolved when the full-width at tenth maximum (FWTM) of the Compton band coincides with the lower limit of the FWTM of the elastic peak. Having determined the minimum acceptable coherent-Compton separation in this way, the

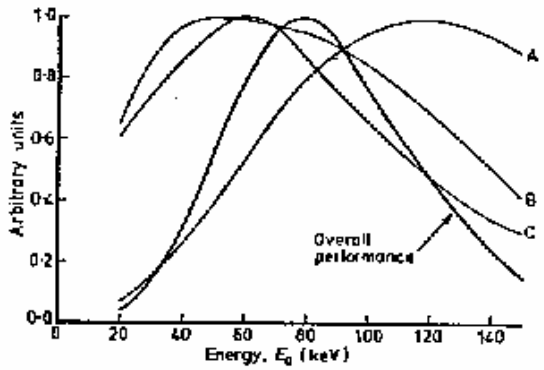

Fig. 5.30. The energy dependence of the performance of a system (Kerr et al. (ref. 15)) for the measurement of TBMD based upon the R/C.T.. Energy dependence of: A the number of coherently scattered photons per unit dose; B the detector counting efficiency; C the mass absorption coefficient for bone.

showed that the principal parameter to be optimized is the precision (see Eq. (15)) that simultaneously includes the counting rate and the sensitivity. Their conclusions were that the optimising procedure proposed by Kerr et al. must be completed by taking into account the changes in sensitivity and precision observed at higher momentum transfer values. Many of the theoretical results of these works have been reported in section 5.2.3. Finally, these authors clearly pointed out the importance of the geometrical counting efficiency that changes considerably at different scattering angles. So far this group is the only one to have published results on the clinical use of the R/C.T. in the measurement of TBMD. Using a 71 degrees angle and a 1.2 Ci americium-241 source they obtained an accuracy of 5% and a precision of 3% with a counting time of 15 minutes. The dose to the patient is about 300 mRad. Figure 5.31 shows a comparison between bone mineral density determined by R/C.T. and that measured directly (ref. 55).

Gigante and Sciuti (ref. 43) extended the analysis of the above mentioned group (refs. 28, 54) showing that a backscattering geometry can optimize the system performance in term of precision at a given counting statistic. Studies on the s.v. shape and on the behaviour of the selfabsorption function in a backscattering geometry, were also carried out.

An interesting development from an instrumentation point of view is that illustrated by Punmalainen et al. (ref. 56) with the use of a X-ray tube in substitution of the less intense radioisotopic sources. The aim of these

corresponding Compton energy shift was then calculated (see E. (1)). With this procedure it is possible to find for a given energy (and known values of the collimation parameters) the minimum scattering angle that can be usefully employed. Figure 5.29 shows the spectrum of photons scattered from a foot using a primary beam energy of 103 keV and a scattering angle of 22.5 degrees. To find the optimal range of primary photon energies the authors studied the energy dependence of: (i) the number of coherently scattered photons per unit mass, (ii) the detector (an intrinsic planar germanium of 400 mm^2 active area) counting efficiency, (iii) differential coherent scattering mass absorption

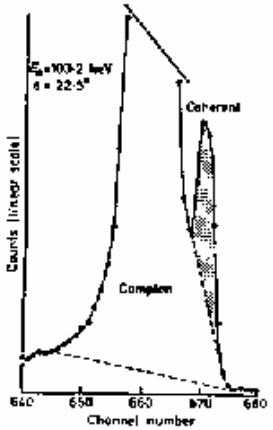

Fig. 5.29. Scattered spectrum from a cadaver foot. (after Kerr et al., ref. 15).

coefficient. From Figure 5.30 that shows the plot of the functions studied by Kerr et al., turns out that an energy around 90 keV is the most favourable.

In 1982 Greenfield et al. (refs. 17, 27, 28, 54) published the results obtained in the measurement of TBMD using americium-241 sources and a larger scattering angle. The authors (ref. 17) discussed the experimental obstacles encountered in the development of a measuring system for clinical use. They showed the advantages of using a 90° geometry in order to obtain a s.v. of more regular shape compared to the elongated forms obtained at smaller angles. These authors, depicted the methodology for studying the different sources of error in an "in vivo" system. In two later reports (refs. 28, 54), they pointed out that the best sensitivities can be obtained either at larger scattering angle for a 60 keV primary beam energy, or generally at higher momentum transfer values (see sections 5.2.2 and 5.2.3). In particular, they

authors was to obtain a more intense primary beam possibly with a tunable energy. The monochromatic beam was obtained using a CsCl filter and a tube tension of 59 Kv_p. They thus obtained a 38.9 keV energy beam useful only for "in vitro" studies. Recently, Timus et al. (ref. 57) with a X-ray tube and the technique of balanced filters obtained a sixty keV beam. They used this to determine the R/C ratios of standard samples obtaining very good results. The availability of more intense X-ray sources as for example the Synchrotron radiation sources (characterized by a high degree of polarization, characteristic that may be usefully used), will certainly give a new impulse to these techniques.

Besides the very interesting application in the determination of TBMD, R/C.T. can be used in other analytical applications for the identification of

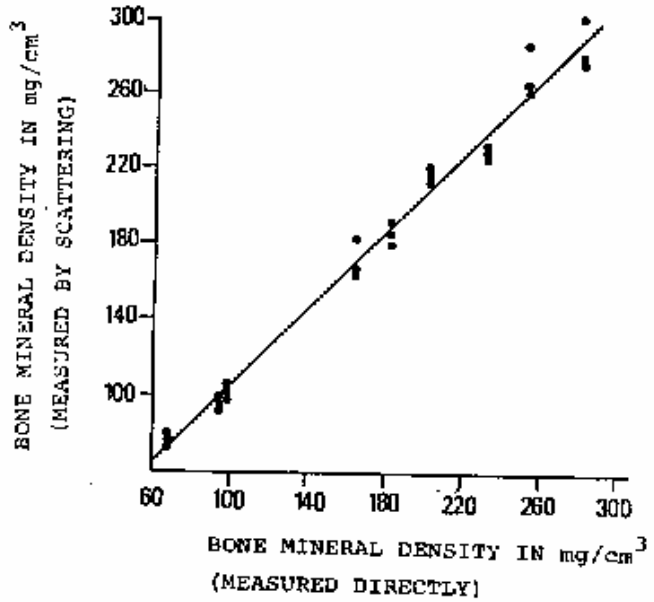

Fig. 5.31. Comparison between the bone mineral density determined by R/C.T. and that measured directly. The regression line is also shown. (After Greenfield et al., ref. 55).

unknown materials and/or in the characterization of tissues. The latter was studied by Holt et al. (ref. 58) using a spectrometer devoted to Compton profile analysis (ref. 59). This spectrometer uses a 5 Ci americium-241

source and a 171 degrees scattering angle. The results demonstrated that accurate characterization of the tissues through the determination of their R/C ratios, can be obtained. Table 5.4 shows the R/C values reported in this work, as measured in different tissues and low Z samples.

TABLE 5.4

The R/C values measured in different tissues and low Z samples.

Sample	R/C x 10^{-3}
De-ionized water	1.023 + 0.017
0.9% saline solution	1.210 + 0.017
Breast cyst fluid	1.161 + 0.017
In-tissues liver*	1.246 + 0.017
In-tissue liver+	1.277 + 0.017
Homogenised liver*	1.180 + 0.031
Homogenised liver+	1.197 + 0.031

* Taken from rats treated with saline solution
\+ Taken from rats treated with phenobarbitol (80 mg/kg solution)

Other measurements carried out with saline solutions up to 20% have shown that R/C.T. has a good sensitivity, in fact a change of 0.2% in concentration gives a measurable 2.5% change in the intensity ratio. Bolt et al. (ref. 58) underlined that in order to obtain such good results, a careful study of the Compton profiles is necessary to minimize the errors in the R/C ratio measurements.

Several investigations have been carried out on the analytical power of R/C.T. in the identification of low Z compounds and in the analysis of metal alloys.

Cesareo (ref. 60) demonstrated the potentialities of this technique in the analysis of binary silver alloys. Later, Gigante and Sciuti (ref. 27) used simultaneously both the informations coming from the scattering and fluorescence components. The XRF spectrum is available only if some elements in the sample emit fluorescence photons of sufficiently high energy, i.e. comparable to that of the scattered photons. The two components are in many cases complementary. This strategy is particularly useful in the analysis of tertiary and quaternary alloys, possibly using scattering intensities from the same material at different primary beam energies (ref. 61). Furthermore, some authors have shown that identification of low-Z material is possible using only the R/C ratio (ref. 27). The calculated values of the scattering intensity ratio are compared in Figure 5.32 with those measured with a spectrometer, using a backscattering geometry and two americium-241 sources as depicted in Figure 5.14. The theoretical values were calculated from the data of Hubbell et al. (ref. 19). Gigante and Sciuti (ref. 27) have shown that identification of a sample is possible using the theoretical R/C ratio values for the single element and a specific computer programme. Corrections for the attenuation effects can be introduced using the tabulated values of the attenuation coefficients.

Manninen et al. (ref. 29) first, and later Manninen and Kolkkalainen (ref. 31) offered an alternative, namely the possibility to define an effective atomic number. They carefully studied the behaviour of the R/C ratio as a function of Z, both for pure elements and low-Z compounds. Using the Equation (12) they found that a good agreement between calculated and measured R/C values can be obtained for an energy of 60 keV and large scattering angles.

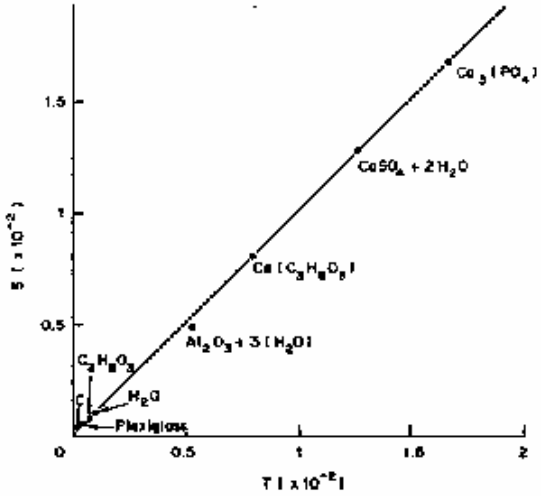

Fig. 5.32. Measured vs calculated R/C ratios for different compounds. (After Gigante e Sciuti, ref. 27).

These results show that for such energy and large angles, there is a dependence of the coherent scattering on Z^3 and of the Compton scattering on Z. Figure 5.33 shows the results obtained by these authors at different scattering angles. The measured Za values differ from the calculated ones (using Eq. (12)) by less than 0.5%.

The analytical potentialities of R/C.T. are clearly shown by the above reported results. The sensitivity of this technique is very good both in the determination of the TBMD "in vivo" and in the identification of tissues and materials. Further improvements are possible using more intense monochromatic sources and faster counting chains. In the near future, R/C.T. will surely become one of the most used techniques of tissue characterization and bulk analyses.

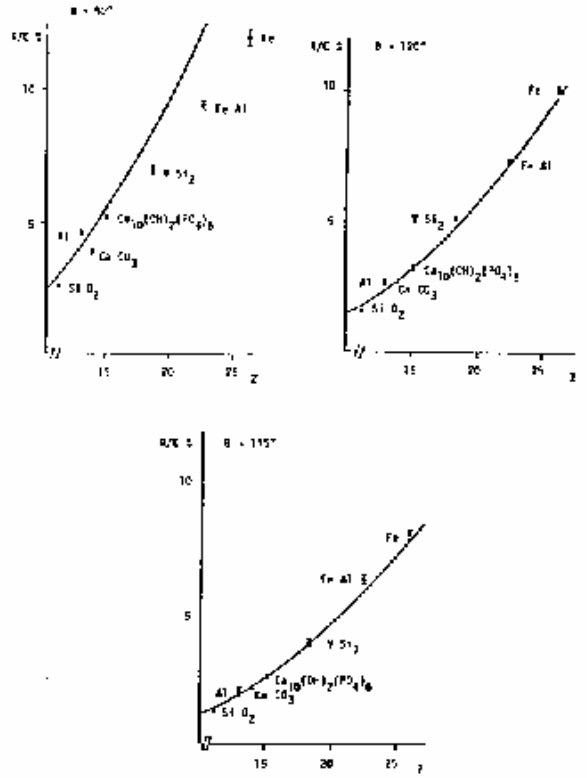

Fig. 5.23. The measured R/C ratios for various compounds, for a primary beam energy of 60 keV and different scattering angles.

ACKNOWLEDGMENTS

The author is deeply grateful to Prof. S. Sciuti for his continuous support and advice in research on PST, and his critical reading of the text and Mr. D. Tursilano for his technical assistance.

REFERENCES

1 R.L. Clarke and G. Van Dyk, Phys. Med. Biol., 18 (1973) 532.
2 R.S. Garnett, T.J. Kennett, D.B. Kenyon and C.E. Webber, Radiology, 10 g (1973) 209.
3 C.E. Webber and T.J. Kennett, Phys. Med. Biol., 21 (1976) 760.
4 H. Olkkonen and P. Karjalainen, Br. J. Radiol., 48 (1975) 594.
5 A.L. Huddleston and D. Bhaduri, Phys. Med. Bol., 24 (1979) 310.
6 A.L. Huddleston and J.B. Weaver, Int. J. Appl. Radiat. Isotopes, 34 (1983) 997.
7 P.G. Lale, Phys. Med. Biol., 4 (1959) 159 and Radiology,
8 R.L. Clarke, E.N.C. Milne and G. Van Dyk, Med. Phys., 3 (1976) 225.
9 F.T. Farmer and M.P. Collins, Phys. Med. Biol., 16 (1977), 229.
10 J.J. Battista, L.W. Santon and M.J. Bronskill, Phys. Med. Biol., 22 (1977) 229.
11 R. Guzzardi, M. Rey, M. Pistolesi, S. Solfanelli a,d C. Ginatini, J. Nucl. Med. Allied Sci., 22 (1978) 11.
12 H. Kunzendorf, Nucl. Instrum. Methods, 99 (1972) 611.
13 P. Punmalainen, A. Uimarihuhta, E.M. Alhva and H. Olkkonen, Radiology, 120 (1976) 723 and P. Puumalainen, H. Olkkonen and P. Sikanen, Int. J. Appl. Radiat. Isotopes, 28 (1977) 765.
14 H.P. Schützler, Int. J. Appl. Radiat. Isotopes, 28, (1979) 115.
15 S.A. Kerr, K. Kouris, C.E. Webber and T.J. Kennett, Phys. Med. Biol., 25 (1980) 1037.
16 J.T. Stalp and B. Mateas, Med. Phys., 7 (1980) 723.
17 S.S. Ling, S. Rustgi, A. Karellas, J.D. Craven, J.S. Whiting, N.A. Greenfield and E. Stern, Med. Phys., 9 (1982) 208.
18 G.A. Carlsson, C.A. Carlsson, K.F. Berggren and R. Ribberfors, Med. Phys., 9 (1982) 868.
19 J.H. Hubbell, W.J. Weigele, E.A. Briggs, R.T. Brown, D.T. Cromer and R.J. Howerton, J. Phys. Chem. Ref. Data, 4 (1975) 471.
20 D.A. Bradley and A.N. Ghose, Phys. Med. Biol., 29 (1984) 1385.
21 F.C. Johns and M.J. Yaffe, Med. Phys., 10 (1983) 40.
22 L. Kissel, R.H. Pratt and S.C. Roy, Phys. Rev. A, 22 (1980) 1970.
23 S.C. Roy, L. Kissel and R.H. Pratt, Phys. Rev. A, 27 (1983) 285.
24 D. Schaupp, M. Schumacher, F. Smend, P. Rullhusen and J.H. Hubbell, J. Phys. Chem. Ref. Data, 12 (1983) 467.
25 A.L. Hanson, Nucl. Instrum. Methods,243 A(1986) 583.
26 S.C. Roy, Nucl. Instrum. Methods, 150 (1978) 283.
27 G.E. Gigante and S. Sciuti, Int. J. Appl. Radiat. Isotopes, 35 (1984) 681.
28 I. Leichter, A. Karellas, J.D. Craven and M.A. Greenfield, Med. Phys., 11 (1984) 31.
29 S. Manninen, T. Pitkanen, S. Koikkalainen and T. Paakkari, Int. J. Appl. Radiat. Isotopes, 35 (1984) 93.
30 R.A. Rutherford, B.R. Pullan and I. Isherwood, Neuroradiology, 11 (1976) 15.
31 D.R. White, Phys. Med. Biol., 22 (1977) 219.
32 D.F. Jackson and D.J. Hawkes, Phys. Rep., 70 (1981) 169.
33 S. Manninen and S. Koikkalainen, Int. J. Appl. Radiat. Isotopes, 35 (1984) 965.
34 R.B. Hazess, J.R. Cameron and J.A. Sorenson, Nature, 228 (1970) 771.
35 T.J. Kennett and C.E. Webber, Phys. Med. Biol., 21 (1976) 770.
36 G. Coates and C.E. Webber, Med. Phys., 9 (1982) 478.
37 A.L. Huddleston, D. Bhaduri and J. Weaver, Med. Phys., 6 (1979) 519.
38 R.A. Wolf and T.R. Munro, Int. J. Appl. Radiat. Isotopes, 36 (1985) 97.
39 F. Arinc and R.P. Gardner, J. Radioan. Chem., 54 (1979) 221.
40 F.T. Farmer and M.P. Collins, Phys. Med. Biol., 19 (1974) 808.
41 J.J. Battista and M.J. Bronskill, Phys. Med. Biol., 23 (1978) 23.
42 L. Brateman, A.M. Jacobs and L.T. Fitzgerald, Phys. Med. Biol., 29 (1984) 1353.
43 G.E. Gigante and S. Sciuti, Med. Phys., 12 (1985) 321.

44 K. Heiss, D. Ing, W. Schuster, Radiology, 102 (1972) 611.
45 C.E. Webber, G. Coates, Med. Phys., 9 (1982) 473.
46 R.L. Cox, F.S. Ong, Med. Phys., 4 (1977) 99.
47 L.E. Preuss, D.G. Piper, C. Bugenis, in C.L. Grant, C.S. Barrett, J.B. Newkirk and C.O. Ruud (Eds.), Advances in X-Ray Analysis, Vol. 18, Plenum Press, New York, 1975, 545.
48 P.C. Shrimpton, Phys. Med. Biol., 26 (1981) 907.
49 A.L. Huddleston and J.P. Sackler, Med. Phys., 12 (1985) 13.
50 J.J. Battista and M.J. Bronskill, Phys. Med. Biol., 26 (1981) 81.
51 R. Guzzardi, M. Mey, Phys. Med. Biol., 26 (1981) 135.
52 G. Harding and R. Tischler, Phys. Med. Biol., 31 (1986) 477.
53 P. Puumalainen, S. Olkkonen and P. Sikanen, Nucl. Instrum. Methods, 163 (1979) 261.
54 A. Karellas, I. Leichter, J.D. Craven and M.A. Greenfield, Med. Phys., 10 (1983) 605.
55 M.A. Greenfield, J.D. Craven, S.S. Shukla, A. Karellas and I. Leichter, Medical and Biological Engineering and Computing, 23 (Suppl.) (1985) 1074.
56 P. Puumalainen, A. Uimarihuhta, S. Olkkonen and E.M. Alhva, Phys. Med. Biol., 27 (1982) 425.
57 D.N. Tiana, M.J. Cooper and R.S. Holt, J. Phys. E: Sci. Instrum., 20 (1987) 35.
58 R.S. Holt, K. Kouris, M.J. Cooper and D.F. Jackson, Phys. Med. Biol., 28 (1983) 1435.
59 M.J. Cooper, Contemp. Phys., 18 (1977) 489.
60 R. Canaveo, Nucl. Instrum. Methods, 179 (1981) 565.
61 G.E. Gigante, L.J. Pedraza and S. Sciuti, Nucl. Instrum. Methods, 12 B (1985) 229.